Received: 12 September 2019 | Revised: 5 March 2020 | Accepted: 16 March 2020 | Published on: 20 April 2020

DOI: 10.1002/qj.3790

Quarterly Journal of the Royal Meteorological Society RMetS

RESEARCH ARTICLE

Evaluating the GECCO3 1948–2018 ocean synthesis – a configuration for initializing the MPI-ESM climate model

Armin Köhl

Institute of Oceanography, CEN, University of Hamburg, Hamburg, Germany

Correspondence
A. Köhl, Institute of Oceanography, CEN, University of Hamburg, 20146 Hamburg, Germany
Email: armin.koehl@uni-hamburg.de

Funding information
German Ministry for Education and Research (BMBF), Grant/Award Number: 03F0824B

Abstract

The paper describes an update of the GECCO (German contribution to the Estimating the Circulation and Climate of the Ocean project) ocean synthesis, now in its version 3, and provides an evaluation of the results with assimilated and independent data. GECCO3 covers the 71-year period 1948–2018 and differs from its predecessor by returning to a single assimilation window instead of partitioning the period in 5-year-long overlapping windows which was previously necessary to yield convergence. A solution to the convergence problem is presented. GECCO3 is intended to be used for the initialization of coupled climate models and is configured for the higher-resolution version of the earth system model (MPI-ESM) developed at the Max Planck Institute for Meteorology. It uses the bathymetry and grid of the MPI-ESM with quasi-uniform resolution of 0.4°, thereby providing the first global eddy-permitting synthesis based on the adjoint method. The synthesis additionally features the estimation of various mixing parameters and can regionally choose between explicit or parametrized eddy fluxes. Except for the altimeter data in tropical regions, GECCO3 is in better agreement with the assimilated data than GECCO2. The improvements relative to the *in situ* data partly result from the much larger amount of Argo data, which show lower model–data differences. Global heat content changes are in good agreement with recent estimates, but show uptake almost exclusively in the top 700 m. An alternative version of GECCO3, created by starting from different first-guess control parameters, was used to evaluate the uncertainty of the estimated parameters and state due to lack of convergence. This estimate suggests a large uncertainty related to the uptake of heat into the lower layers, while estimates of mean meridional transport of heat and freshwater are not affected.

KEYWORDS

climate model initialization, eddy-permitting ocean synthesis, heat content change, ocean transports

1 | INTRODUCTION

Ocean syntheses (also referred to as ocean reanalyses) created by the combination of dynamical information from ocean models with observational data in a step called data assimilation are used to retrieve a complete picture of the changing ocean–sea ice system. Nowadays, many different products are available with different virtues and different problems. In the framework of the Ocean Reanalyses Intercomparison Project (ORA-IP), a fairly complete overview of currently available global products was presented by Balmaseda *et al.* (2015), who also provide an initial assessment of the consistency of several key parameters derived from these products. More in-depth analyses of various parameters ranging from mixed-layer depth, heat content, and sea level through surface heat flux and Atlantic Meridional Overturning Circulation (AMOC) to salinity and sea ice followed shortly afterwards (Chevallier *et al.*, 2017; Karspeck *et al.*, 2017; Palmer *et al.*, 2017; Shi *et al.*, 2017; Storto *et al.*, 2017; Toyoda *et al.*, 2017; Valdivieso *et al.*, 2017).

Among those products, most syntheses rely on sequentially gathering information from a model prediction which is periodically combined with data information in an analysis step. The analysis step in these sequential methods rely on the estimation of error covariances, which are approximated by different methods ranging from optimal interpolation through 3D-Var to ensemble Kalman filter methods. Only a small number of products rely on the adjoint method, which minimizes the weighted difference between model and data over a period of time by adjusting several control variables in an iterative manner. Among the latter systems are the GFDL (Geophysical Fluid Dynamics Laboratory) Modular Ocean Model-based K7-products (Sugiura *et al.*, 2008; Masuda *et al.*, 2010) and the MITgcm model-based ECCO-v4 (Estimating the Circulation and Climate of the Ocean; Speer and Forget, 2013; Wunsch and Heimbach, 2013a; Forget *et al.*, 2015) and GECCO (German contribution to ECCO) syntheses (Köhl and Stammer, 2008; Köhl, 2015). Sequential methods carry model and data information only forward in time, while smoother methods such as the adjoint method also carry information backward in time. The main difference between sequential and adjoint methods is that in the latter the state is adjusted indirectly through the parameters while in the former the state is directly adjusted. The adjoint method is therefore less sensitive to data gaps but the limited control parameter space may not suffice to correct for model biases even for high data density. The present paper focuses on the presentation and evaluation of a new version of the GECCO product and will also address some difficulties encountered during the production of the latest product. GECCO2 showed convergence problems, which were solved by splitting the period into 5-year-long overlapping windows. Since the splitting created artificial 4-year cycles (also https://icdc.cen.uni-hamburg.de/1/daten/reanalysis-ocean/gecco2.html; accessed 27 March 2020), this solution will not be followed here. Instead, we present the cause of the loss of convergence over long assimilation periods and how it can be avoided.

Ocean syntheses generated by assimilating observations into ocean models are used as initial conditions for seasonal to decadal predictions. As syntheses are often created by using stand-alone ocean models with configurations different from the climate model used for prediction, the information usually needs to be transformed to fit the grid of the climate model. The necessary interpolation leads to gaps in the closure of the temperature and salinity budgets and the resulting trends were shown to reduce decadal prediction skills (Kröger *et al.*, 2018). To avoid interpolation, the new version of GECCO will be configured on the grid and bathymetry of the ocean component of the earth system model developed at the Max Planck Institute for Meteorology (MPI-ESM; Giorgetta *et al.*, 2013). The considered higher-resolution version of MPI-ESM features a quasi-uniform resolution of 0.4°, which is isotropic in the Southern Hemisphere but has two dislocated poles in the Northern Hemisphere and is termed by (Jungclaus *et al.*, 2013) as eddy-permitting for most regions. In comparison to GECCO2, the set of control parameters includes additional mixing parameters to reduce the bias of the model and to provide estimates of mixing processes. The new product also includes now relaxation to surface salinity, which makes the previously employed separation into 5-year-long windows obsolete and the new synthesis returns to an optimization over the complete period, as previously employed by GECCO.

As before, the results of the syntheses are available at https://icdc.cen.uni-hamburg.de/daten/reanalysis-ocean/gecco3.html, which also provides further technical details about the variables. We will discuss the configuration of the new version in Section 2. Section 3 describes the optimization process and Section 4 attempts to explore one aspect of the uncertainty of the solution. After an evaluation of the state relative to the assimilated data in Section 5, heat content changes and heat and transport estimates are compared as examples for independent data in Section 6.

2 | METHODS

2.1 | Model configuration

As for the previous synthesis GECCO2, the new version of the synthesis (GECCO3 in the following) covers the

years of the National Centers for Environmental Prediction (NCEP) RA1 reanalysis (Kalnay *et al.*, 1996), which now extends over the period 1948–2018. Differently from GECCO2, GECCO3 uses only one assimilation window covering the full period. The update is based again on the MITgcm ocean model (Adcroft *et al.*, 2002) coupled to a dynamic viscous-plastic sea ice model (Losch *et al.*, 2010) but, as in the previous update, the horizontal resolution was further increased. The horizontal and vertical discretization and the bathymetry were taken from the MPI-HR configuration of the MPI-ESM climate model (Jungclaus *et al.*, 2013). The associated TP04 grid has a nominal horizontal resolution of 0.4° and 40 levels increasing from 12 m at the surface to 600 m at depth. The bottom cell is realized as a partial cell. Certain editing of the bathymetry in comparison to a realistic topography was noticed, notably the widening of the Faroe Bank Chanel (FBC) and a reduction of the depth north of the Florida Strait. The impact of the former is a larger transport through the FBC and a smaller Denmark Strait overflow transport in comparison to observations. The latter depth reduction limits the Florida Strait transport to a range of 20 to 22 Sv. Although these disadvantages were noticed before the assimilation, since one of the purposes of the GECCO3 synthesis was to provide compatible initial conditions for initializing decadal hindcasts with the MPI-HR model, for the sake of preserving the compatibility the bathymetry was adopted without changes. As before, parametrizations include a dynamic/thermodynamic sea ice model, the K-profile parametrization (KPP) mixed-layer model (Large *et al.*, 1994) and despite permitted eddies the Gent and McWilliams (1990) (GM) parametrization of eddy tracer fluxes and isopycnal diffusion (Redi, 1982). Surface fluxes are derived by the model via bulk formulae (Large and Yaeger, 2004) and the sea ice model from the atmospheric, oceanic and sea ice state. Freshwater forcing is represented as virtual salt flux. The prior of the atmospheric state is taken from the 6-hourly NCEP data and additional river-runoff from Fekete *et al.* (2002).

2.2 | Control parameters

As before, the adjoint method was employed to bring the model into consistency with the assimilated data and the prior error weights. To achieve this goal, a cost function was formulated as the sum of the quadratic model–data differences divided by the prior error estimates:

$$J = \sum_i [d_i - \mathbf{E_i} y_i]^{\mathrm{T}} \mathbf{R_i^{-1}} [d_i - \mathbf{E_i} y_i] + \sum_j u_j^{\mathrm{T}} \mathbf{Q_j^{-1}} u_j. \quad (1)$$

The cost function J has two parts. The first part measures the model–data misfits $d_i - \mathbf{E_i} y_i$. Here, E_i is the observational operator that maps the model state y_i to the observation space d_i. The second part is the background term, which is necessary for regularization and in which u_j are the deviation of the parameters from their priors. The relative contribution of each term in the cost function is controlled by data error weight $\mathbf{R}^{-1}$ and the weight $\mathbf{Q}^{-1}$ which describes the prior uncertainty of the controls.

The cost function was iteratively minimized by adjusting the control parameters by employing gradients to the cost function, which are calculated with the adjoint model. The set of control parameters include variables of the atmospheric state and besides mixing parameters the initial temperature and salinity. In addition to the previously adjusted surface air temperature, humidity, precipitation, and 10 m wind speeds, the short-wave heat flux and four mixing parameters were included into the control vector. The atmospheric state is externally provided by the NCEP reanalysis and treated as parameters in the bulk formulae. It was adjusted every 10 days. Similar to the study with the original GECCO configuration by Liu *et al.* (2012), the mixing parameter include the isopycnal, the thickness, and the vertical diffusion. In addition to these, the depth-independent critical gradient Richardson number (*Ri*) was chosen to control the mixed-layer depth. The sensitivity to changes of *Ri* was investigate by Zedler *et al.* (2016) as one of the most influential parameters in the KPP mixed-layer parameterization. To ensure positive values, corrections to the diffusivities were formulated by multiplying with the exponential of the parameter, thereby accommodating a wide range of adjustments.

2.3 | Assimilated data and error weights

The set of assimilated data includes along-track altimeter data from Topex/Jason (TP), the European Remote Sensing satellites ERS-1 and ERS-2 and the Environmental Satellite Envisat (the three satellites are referred to as ERS in the following), the Geosat Follow-On mission (GFO) and Cryosat-2 (C2) and is used to constrain the sea surface height (SSH) anomalies in the period after 25 September 1992. As the model employs the Boussinesq approximation, its global mean sea level is constant and the global mean estimated from mapped altimeter data was subtracted from the along-track altimeter data. For both types of altimeter data, reprocessed data were used as far as possible, and to fill in the missing data during the last six months, near-real-time data were used. HadISST (Rayner *et al.*, 2003) is used to constrain the sea surface temperature (SST). It was set to freezing temperatures beneath non-zero sea ice concentrations taken from

TABLE 1 Configuration of the experiments

Experiment	Data assimilation	Tracer advection scheme	Relaxation time-scale
GECCO3first	yes	centred with GM	no relaxation
GECCO3	yes	centred with GM	60 days
GECCO3S6m	yes	centred with GM	180 days
CTRL	none	centred with GM	60 days
CTRL_FLS	none	FLS without GM	60 days

the Version 1 Ocean and Sea Ice Satellite Application Facility (OSI SAF) High-Latitude Processing Center. Temperature and salinity profiles are taken from the EN.4.2.1 data base (Good *et al.*, 2013) with the Gouretski and Reseghetti (2010) corrections. Additionally, the mean SSH from the combination of the GOCO05s geoid (Pail *et al.*, 2010) with the DTU10 mean sea surface (Andersen, 2010) constrains the mean dynamic topography during the period 1993–2018. The mean SSH was re-referenced to accommodate different averaging periods. Initially, the synthesis was started with the climatological temperature and salinity constraint from the World Ocean Atlas 2013 (Locarnini *et al.*, 2013; Zweng *et al.*, 2013), which was replaced by the World Ocean Atlas 2018 (Locarnini *et al.*, 2018; Zweng *et al.*, 2018) once it became available. The same change applies to the sea surface salinity (SSS) constraint, for which climatological salinity was assimilated as monthly SSS.

Error weights of the data are specified as in Köhl (2015); they are assumed to be diagonal and are dominated by the representation error of the model due to unresolved eddies. For the background information, errors of the atmospheric state are calculated from the standard deviation of the NCEP fields while removing the climatology for air temperature and short-wave heat flux before the calculation because their seasonal cycle is assumed to have a relatively small error. Uncertainties for the exponential factors applied to isopycnal and thickness diffusion are set to 3, which yields roughly a multiplicative factor of 20. The factor is inspired by the range of values covered by independent estimates (e.g., Stammer, 1998; Ferreira *et al.*, 2005; Eden *et al.*, 2007). In comparison to GECCO2, the corresponding background values were reduced from 800 to 500 $m^2 \cdot s^{-1}$ and the horizontal viscosity was also reduced from 10^4 to 2,500 $m^2 \cdot s^{-1}$. The background value of vertical diffusion is 10^{-5} $m^2 \cdot s^{-1}$ and the error for the exponential factor is 5, which yields a multiplicative factor of 150. The factor is inspired by estimates based on shear and stain profiles (e.g., Kunze *et al.*, 2006) considering the fact that locally, for instance in the equatorial thermocline, values as high as 10^{-2} $m^2 \cdot s^{-1}$ can be reached (e.g., Gregg, 1987; Moum *et al.*, 2009; Smyth *et al.*, 2013). The error of *Ri* was assumed to be 0.5. For the mean dynamic topography and the climatological temperature and salinity fields, a constant of 4.5 cm and vertical profiles as in Köhl and Stammer (2008) were used, respectively. Modifications to the adjoint are necessary because of the nonlinearity of the parametrization. These include the removal of the adjoint to the sea ice model and changes to the GM parametrization as described in Liu *et al.* (2012). For changes to the KPP parametrization, the method of Jiang *et al.* (2002) was adopted.

2.4 | The simulations

We describe here five runs (Table 1), which were started on 1 January 1948, from one year of spin-up after initializing from rest, and with temperature and salinity conditions taken from the January fields of the World Ocean Atlas 2013 (WOA13). CTRL is without data assimilation and forced with the 6-hourly atmospheric state from NCEP RA1 employing surface relaxation with a time-scale of 60 days to climatological salinity values from World Ocean Atlas 2018 (WOA18). To evaluate the importance of parametrized fluxes, a further experiment was performed (CTRL_FLS), which differs from CTRL by the use of a flux-limited advection scheme instead of the GM parametrization to provide stability for the low horizontal diffusion.

The first optimization attempt (GECCO3first) with the new set-up did not use relaxation but added during the first three iterations the diagnosed salt fluxes from parallel runs which differ only by additionally including SSS relaxation. Since the fluxes were diagnosed from monthly means and projected on the 10-day corrections, a flux error was inevitable and the twin with relaxation was not reproduced. Although adding the correction fluxes greatly reduced the cost functions, the surface salinity fields stayed close to the twin only for about 20–30 years, and thereafter the two runs diverged. The progress of iteratively reducing the cost stalled at iteration 13, but the

resulting cost function was only slightly lower than CTRL. The premature stalling of the progress and the divergence was attributed to the instability of the model to freshwater perturbations in high latitudes for flux boundary conditions (Bryan, 1986a).

However models are known to be stable under salinity-restoring boundary conditions (Bryan, 1986b). To solve the stability problem and to start with an initial cost function at the same level as CTRL, GECCO3 was chosen to follows the set-up of CTRL with SSS relaxation. To test the sensitivity to the SSS relaxation, at iteration 10 two different optimizations were continued: one with the two-month SSS relaxation time-scale (GECCO3) and a second with a six-month SSS relaxation time-scale (GECCO3S6m).

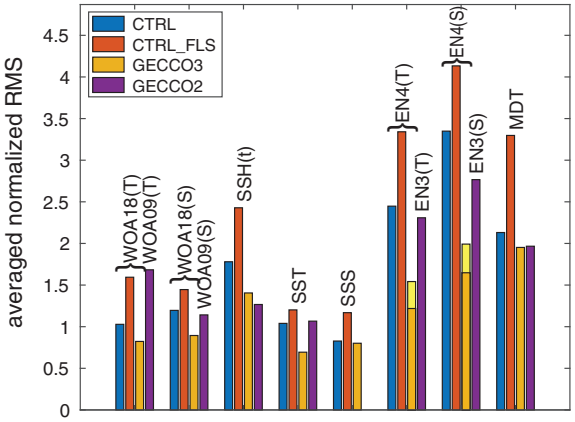

FIGURE 1 Cost function contributions shown as the average root mean square (RMS) value normalized by the prior error. A value of 1 indicates consistency between model, data and the prior error. Differences from EN4 data are evaluated for CTRL as full-field while GECCO3 uses anomalies with respect to the time mean. The contribution from the mean bias is indicated by the bright yellow portion of the EN4 bars for GECCO3. The cost function contributions for GECCO2 are based on a different version of the data as indicated in the figure and are taken over the shorter period 1948–2011

3 | OPTIMIZATION

3.1 | Parametrized versus explicit eddy fluxes

In the MPI-ESM configuration, a flux-limited advection scheme (FLS) is used together with a grid-size-dependent scaling of the GM coefficients which scales the parameters to less than $50\,m^2{\cdot}s^{-1}$ and causes the effect of the parametrization to virtually disappear. As a consequence, the MPIOM ocean model can make full use of the available resolution, and the model is able to simulate meanders and larger eddies. As the present set-up is designed to provide estimates of the GM mixing coefficients and the associated eddy fluxes, the set-up requires parametrized fluxes. The question arises whether parametrized fluxes are still suitable if the model is able to generate limited but explicit eddy fluxes. A suggestion for a transition from parametrized to simulated eddies based on the deformation radius and the grid size was proposed by Hallberg (2013). Since the mixing parameters are part of the control, the method can reduce the mixing parameters and use fluxes from explicit eddies instead of parametrized fluxes. However, the method also adjusts individual eddies to reduce the eddy-related contribution despite less realistic resulting eddy fluxes.

Since the two options of the model to realize eddy fluxes are at the opposite sides of the GM parameter range, the associated cost function may have two local minima on the two sides of the range. The initial parameter choice is therefore crucial and the best choice can objectively be assessed in the context of the data assimilation set-up by comparing the cost function of CTRL with that of CTRL_FLS, which does not employ GM parametrization similar to the MPI-ESM. The results of this comparison are shown in Figure 1. Apparently, parametrized eddies provide substantially lower model–data differences for all data types. Since mismatching eddies will produce on average larger RMS differences than the same state without eddies, the state with lower differences and parametrized fluxes may actually not be more realistic. However, the argument is much less valid for the contribution from the climatologies, for which 71 model months were averaged. As the key objective of the adjoint method is to minimize the cost function, the GM parametrization was employed.

3.2 | Changes during the course of the optimization

GECCO3 is the synthesis as described above, and we analyze here the state after 41 iterations, over which the cost was reduced to 41%. All analyses are performed over the entire period 1948–2018 unless otherwise specified. Over the course of the iterations, a few changes have been introduced to the set-up, which are illustrated in Figure 2 and which should be explained here. The optimization procedure was started as a synthesis over the period 1948–2017 with two-month SST and SSS relaxation. As explained above, a second synthesis (GECCO3S6m) branched off at iteration 10 by increasing the relaxation time-scales to 6 months (green curve), and at iteration 16 the SST relaxation was omitted in both syntheses with very little impact on the SST cost contribution. Beyond iteration 20, the progress for GECCO3 became small, allowing

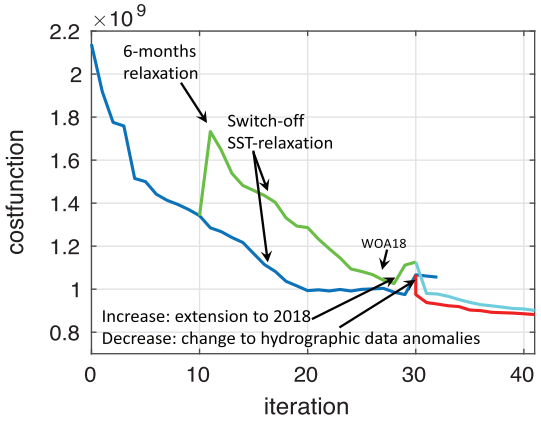

FIGURE 2 Cost function reduction of the two syntheses with associated changes in the configurations. Both configurations start from the set-up using SST and SSS relaxation with a two-month time-scale. GECCO3 follows the blue and then the red line after switching the treatment of *in situ* data to the assimilation of anomalies. GECCOS6m branches off as green line and follows as cyan after the switch. The syntheses were extended to include 2018 as soon as the data became available, which happened at different iterations for GECCO3S6m and GECCO3

GECCO2S6m to catch up. The climatology was updated from WOA13 to the preliminary version of WOA18, when it became available at iteration 26 (the preliminary version of WOA18 differs from the final product mainly in the upper few hundred metres visible as eddy-like features and at places around Greenland, Baffin Island and on the shelf in the Arctic). The syntheses were extended until the end of 2018, once the complete EN4 data for 2018 became available. At this time the progress had also slowed down for GECCO2S6m, and the treatment of the assimilation of the *in situ* data was changed to allow for further improvement. Initially, full *in situ* data were assimilated, such that the reduction in bias or mismatch in variability reduces the cost. However, as noted by Köhl *et al.* (2012), the bias contributes considerably to the cost, and if it persists, can hinder matching the variability. For the last iterations, we followed their approach and changed to the assimilation of anomalies relative to WOA18 at iteration 30. The notable decline in cost is related to the remaining mean bias relative to the *in situ* data at that iteration. After the change of set-up, a further 10% reduction was possible, during which particularly the altimeter cost was reduced.

4 | UNCERTAINTY QUANTIFICATION

For the optimization, no formal termination criterion was employed. Instead, the optimization was terminated when further progress became too slow to justify the expended computation time (about 0.4% reduction for the final iteration). Instead, the justification for the product, as detailed in the following section, is the reduction in misfit and the achieved level of consistency. Given the large control vector ($\mathcal{O}(10^9)$), the limited number of iterations do not facilitate convergence, which implies a dependence of the result on the starting point and uncertainty of the state and parameter estimation associated with this.

To be useful, every estimate requires an uncertainty quantification, which in the case of the adjoint method can formally be derived from the inverse of the Hessian matrix of cost function near the minimum (Thacker, 1989). Although approximations of the Hessian are calculated as part of the employed quasi-Newton optimization algorithm M1QN3 (Gilbert and Lemaréchal, 1989), experience with evaluating the associated Hessian approximation revealed little changes of the off-diagonal elements relative to the initial assumption. Consequently, the resulting uncertainty estimate is doomed to be too dependent on the initial guess to be useful. Since exact calculations as recently presented by Kalmikov and Heimbach (2014) are extremely costly, and may for nonlinear models only be valid if a state close to the minimum was found, we use the two alternative estimates GECCO3 and GECCO3S6m to provide at least an idea how much the lack of convergence may affect the results.

In the following, both estimates are treated as equivalent approximations to the optimal state as almost identical cost function contributions are ultimately achieved. The difference in their relaxation time-scale induces a freshwater flux perturbation at iteration 10, which causes the two estimates to take different optimization routes towards the minimum. The missing part of the relaxation flux in GECCO3S6m can be explicitly represented by changes in precipitation. Only the cost function contributions directly associated with the freshwater fluxes (humidity and precipitation) differ, but since they account together for less than one in 10,000 and are only about 10% larger for the low-relaxation case, the two solutions can be considered as alternative approximations to the solution of basically the same optimization problem.

A direct comparison of the differences due to lack of convergence to the formal uncertainty estimate is possible for the Drake Passage transport. Kalmikov and Heimbach (2014) reported a posterior uncertainty of 2.5 Sv estimated by inverting the Hessian of the misfit function of a global idealized barotropic model. In comparison, the transport time series of GECCO3 and GECCO3S6m differ by a RMS value of 2.4 Sv. This means the uncertainty in determining the minimum by a limited number of iterations is already as large as the estimated posterior uncertainty in a simple model. Although the differences between GECCO3

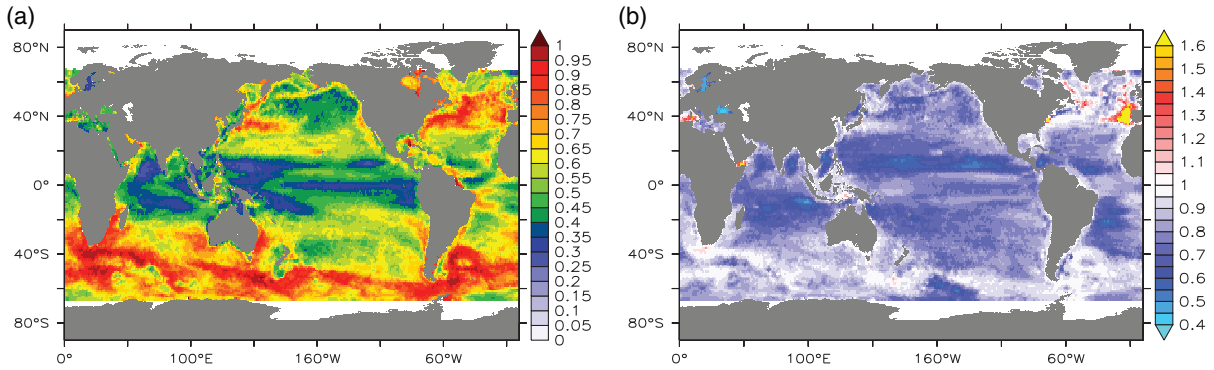

FIGURE 3 (a) RMS difference between GECCO3 sea level anomalies and the along-track Topex/Jason data weighted by the square root of the sum of the SSH variances from GECCO3 and the altimeter data. A value of 1 corresponds to a model that is not better than white noise. (b) Ratio of the RMS differences between Topex/Jason and GECCO3 over the RMS differences between Topex/Jason and CTRL. To improve the visual impression, missing values have been filled with a Gaussian interpolation. The equivalent figure for ERS/Envisat/C2 is very similar with on average 2.3% higher values

and GECCO3S6m cannot be treated as an uncertainty estimate, results of both syntheses are presented together in the following to provide an idea of how vulnerable the estimate can be to small changes of the initial parameters.

5 | MODEL–DATA DIFFERENCES

Ultimately, the success of the assimilation is measured by achieving consistency between model, data and the prior error information. Since in the cost function the model–data differences are divided by the prior error and after squaring summed up, one expects for consistency that on average each data point contributes a value of 1 to the cost. The model–data difference would then be the same as the prior error. Dividing their cost contribution by the number of observation and taking the square root provides a metric for how large the model–data difference is on average in the units of the prior error. A value of 1 is expected for consistency. The contributions to the cost and their reduction in this metric are shown in Figure 1 for GECCO3. For GECCO3S6m the contributions are nearly identical (not shown), except for SSS, whose value is nearly as high as for CTRL. GECCO3 reaches values below one for the climatological T and S and SSS and SST. For these contributions, CTRL was already near consistency and better than or equal to GECCO2. Altimeter and *in situ* data anomalies range near 1.5. Only the MDT reaches up to 2 and only the altimeter data show higher values than GECCO2. However, in GECCO2 SSH anomalies were defined relative to a 5-year mean, while in GECCO3 they are relative to a 26-year mean. Long-term variability of the mismatch is therefore filtered out in the GECCO2 set-up. The largest improvement over the course of the optimization, but also relative to GECCO2, is noted for the EN4 *in situ* data. The contributions are about 0.75 lower than for GECCO2. The higher resolution is certainly one factor as the agreement with the climatology shows; however, also important is the larger amount of Argo data (only until 2011 in GECCO2), which on average has lower differences from the model as detailed below.

Cost function contributions provide only a global number characterizing the misfit, which regionally is very different because the errors are typically large where the signal is large and because the models have distinct regional biases. To take the effect of varying sizes of variability into account, the RMS differences of GECCO3 to the Topex/Jason SSH are shown in Figure 3 divided by the square root of the sum of the variances from GECCO3 and the altimeter data . The same has been done for GECCO2 before, such that the figures can be directly compared (figure 6 in Köhl 2015). Overall similar patterns are found for GECCO2 and GECCO3. The best match with the data is in tropical latitudes and large errors that reach the size of the variability exist in the North Atlantic and the Southern Ocean. While GECCO3 does not quite reach the match in tropical regions, differences to the data are smaller in midlatitudes, particularly in the eastern North Pacific where GECCO2 worsened in comparison to its control.

Instead of showing also the misfit for CTRL, we show in Figure 3b the ratio of the respective RMS differences to better highlight regions of improvement or degradation. The match improved almost everywhere, in particular along the North and South Equatorial Currents. The eddy-rich Southern Ocean and regions of other energetic boundary currents hardly improve, since errors are dominated by eddies that are not well represented or cannot be matched. By contrast, a distinct problem exists as before in GECCO2 in the eastern part of the North Atlantic off the coast of Portugal. This is a region of

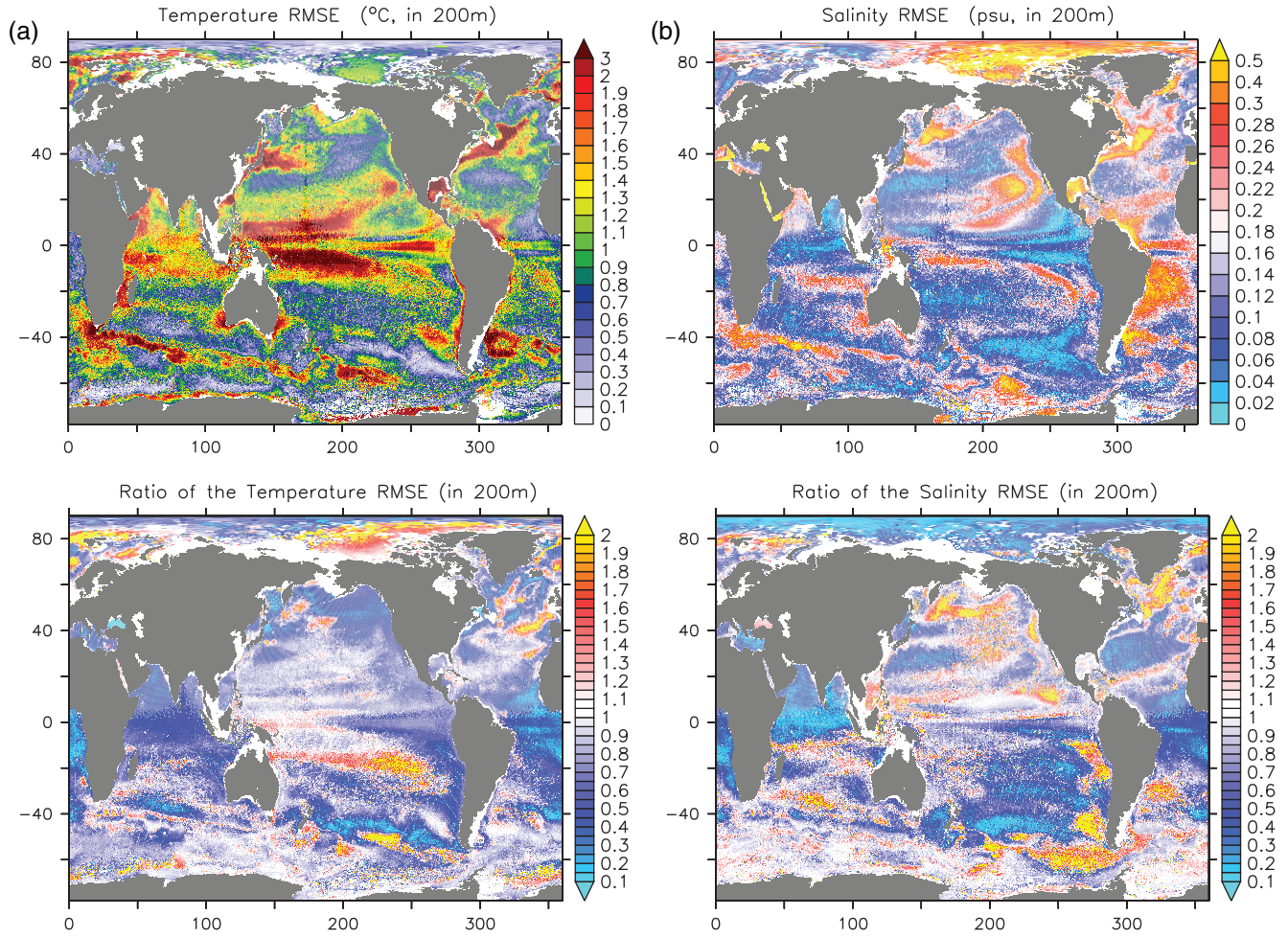

FIGURE 4 (a, b) RMS differences between GECCO3 and the EN4 data for (a) temperature and (b) salinity at 200 m depth and (c, d) the ratio of the RMS differences between GECCO3 and EN4 to the RMS differences between between CTRL and EN4 for (c) temperature and (d) salinity at 200 m depth

relatively low variability, in which GECCO3 generates substantially more variability. The adjoint method transports model–data mismatch information upstream, which is upstream of the currents but also upstream of the propagation of waves. Since substantial variability and mismatch exist in the region of the Gulf Stream due to eddies and meanders that cannot be matched, this information moved eastward but also northward along the Labrador Currents and creates erroneous variability visible there.

RMS differences to the EN4 data are shown in Figure 4 as before for GECCO2 at 200 m depth to allow a direct comparison. The majority of colour scales cover now only about half the range than before to provide more details for regions of smaller misfits. Patterns of misfit are very similar to those of GECCO2 with smaller amplitudes consistent with the reduced cost function values in comparison to those of GECCO2. As before, a large fraction of the misfit is related to a persistent bias (not shown), which is also reduced in comparison to GECCO2, in particular along the northern flank of the Antarctic Circumpolar Current (ACC). A noticeable difference to GECCO2 is the existence of values in the Arctic thanks to the program of ice-tethered profilers. For temperature, additional signatures of higher misfit are visible in the equatorial region of the North Atlantic, where the level of misfit is in the range of the previous control.

Nevertheless, the ratio of the RSME values between GECCO3 and CTRL reveals the equatorial region of the North Atlantic as the one with the largest improvements, suggesting that the new configuration does not perform well in this region. In addition to this, the ratio reveals larger improvements in the South Atlantic, Indian Ocean and along the northern flank of the ACC, while there is some increase in misfit noticeable along the southern flank. Further regions of increased misfit exist in some parts of ice-covered regions and the region of the South Equatorial Current of the Pacific.

The agreement in pattern with a larger misfit in the equatorial Atlantic also holds for salinity. Higher values are visible along the California Current and its extension

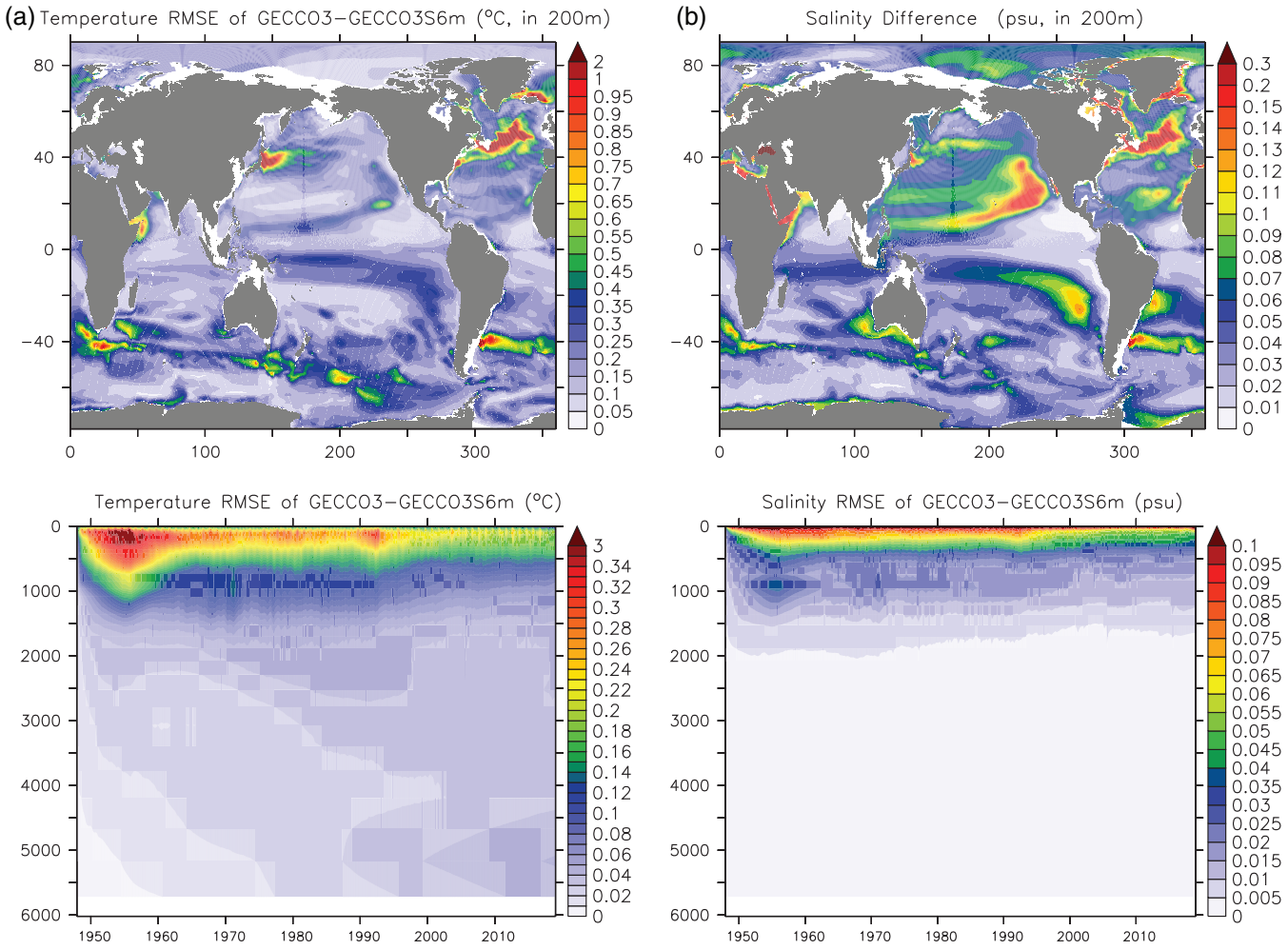

FIGURE 5 RMS differences between GECCO3 and GECCO3S6m for (a) temperature and (b) salinity at 200 m depth and as horizontal averages versus depth over the period 1948–2018

into the North Equatorial Current (NEC). However, further downstream of the NEC the misfit in the western Pacific is greatly reduced. The longer assimilation window in GECCO3 in comparison to GECCO2 may have facilitated the reduction but, by transporting the information further upstream, created the large misfit in the eastern Pacific. This general pattern is also visible when comparing GECCO3 to CTRL by their misfit ratio. In the Pacific, regions of degradation exist mostly near the eastern boundaries. These are the regions where the misfit information accumulates when transported by eastward propagating Rossby waves (in the backward-in-time running adjoint model).

Although the RMS differences to the data look very similar for GECCO3 and GECCO3S6m, the RMS differences between the syntheses (Figure 5) are similar to those of the differences between synthesis and data. Regions of large differences for temperature as well as salinity are the most energetic regions, such as the boundary currents and the ACC. These regions are characterized by eddies and meanders that are not predictable and thus not controllable by estimating parameters through the adjoint method. In these parts, differences reach 1°C and 0.1–0.2 practical salinity units (PSU). Further noticeable regions are the eastern, equatorward edges of the subtropical gyres. These regions are characterized by baroclinically unstable long Rossby waves that show a clear signature in the adjoint sensitivities (e.g., Galanti and Tziperman, 2003; Köhl, 2005); small disturbances tend to grow there, which render the states to be hard to predict or control. In comparison to the energetic regions, differences are typically lower in temperature, reaching only 0.2–0.5°C, but are at about the same level for salinity.

Figure 5c,d show the evolution of the RMS differences between GECCO3 and GECCO3S6m for temperature and salinity. There is a fast increase in RMS differences noticeable during the first five years, followed by a reduction that happens roughly in two steps. Differences peak at 200 m for temperature and at the surface for salinity. The largest differences are seen during the first 10 years, in

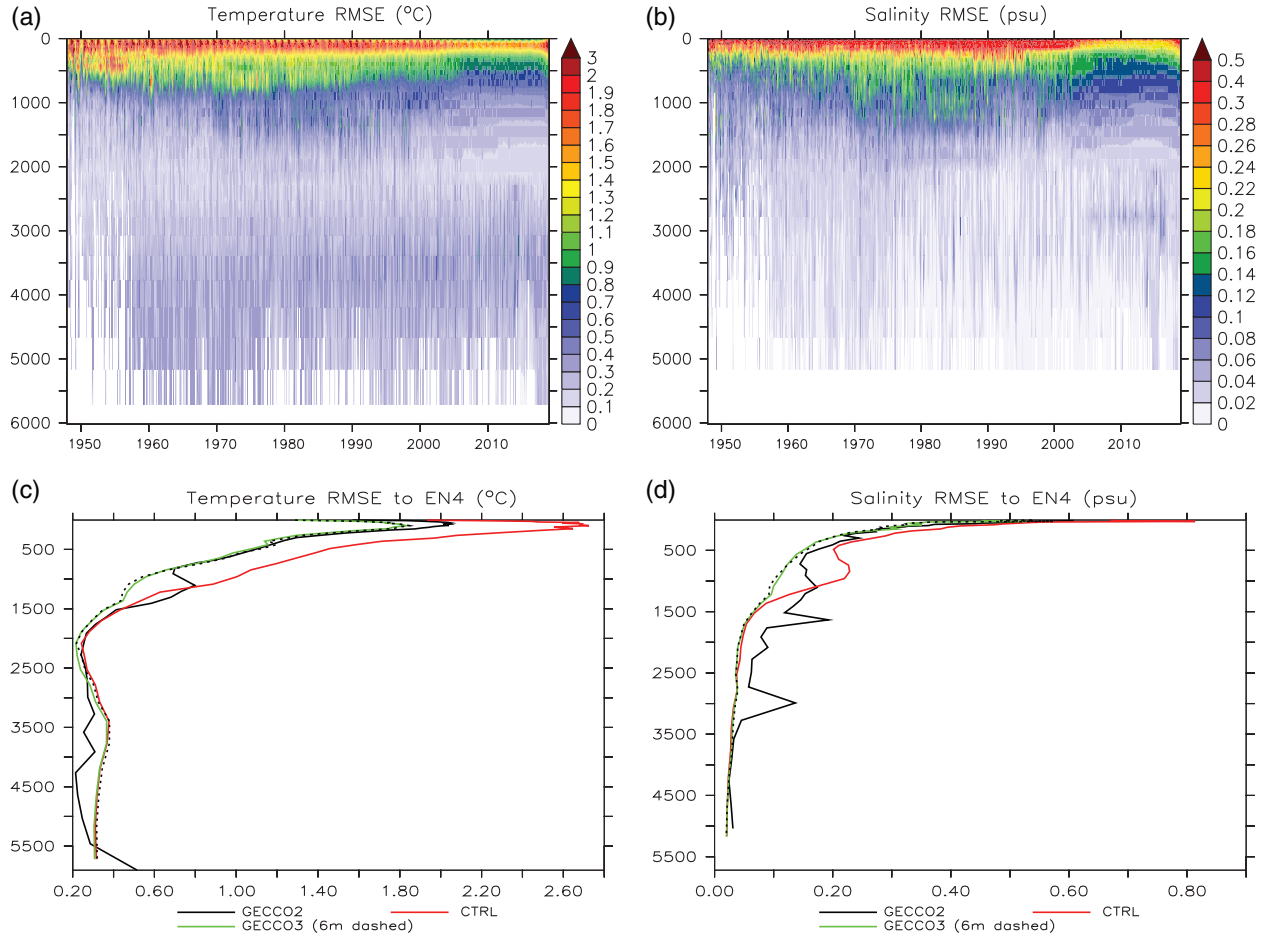

FIGURE 6 Time series of the square root of the horizontally averaged squared (a) temperature and (b) salinity differences to the EN4 data for the upper 6,000 m from GECCO3. (c, d) Square root of the time mean of horizontally averaged squared (c) temperature and (d) salinity differences to the EN4 data. GECCO3S6m is shown as dotted curve.Each year has the same weight despite the much higher data density during the Argo period. The larger RMS differences during the pre-Argo period leads to overall larger RMS error values than just averaging over all data points, but the metric is less biased by data sampling

which spin-up effects are important. The following period of relatively stable differences is characterized by maximum values of 0.25–0.30°C in temperature and 0.1 PSU in salinity. This period ends with the advent of altimeter data, which leads to decreasing differences which reach maximum values below 0.22°C and 0.08 PSU, respectively. In comparison to the introduction of altimeter data, the introduction of the Argo data leads only to a very small further reduction of the differences noticeable for the years roughly following 2005. Although the sensitivity to the relaxation time-scale provides only an indication of the uncertainty of the estimate, the comparison shows the profound effect of especially the altimeter data, and that the period before 1993 is noticeably less well constrained, particularly during the spin-up period.

Profiles of the time evolution of the RMS difference to EN4 are shown in Figure 6 for temperature and salinity. Both show a clear reduction in misfit in the upper 1,000 m with the advent of the Argo data around 2003 with an even more pronounced transition in the near-surface layers for salinity. The decrease is unlikely to be attributed to changes in data quality since observational errors are much smaller than the representation error of the model. Smaller residuals benefit from the more uniform sampling by the Argo profilers since they sample equally well the quieter areas away from the energetic regions that drew more attention by field programs. Although the adjoint method is supposed to fit the data best in the middle of the assimilation window, in the range 500 to 1,500 m larger differences are apparent in the period 1970–1990 and between 1995 and 2005. A similar, though deeper, larger signal was visible before in GECCO2 related to the Mediterranean outflow. In GECCO3 the signal is related to large errors along the Gulf Stream and the Northwest Corner area that received more attention by field programs during these periods and which are areas of large misfits.

In Figure 6c,d, the temporal means of the profiles are compared to those of GECCO2 and CTRL. GECCO3

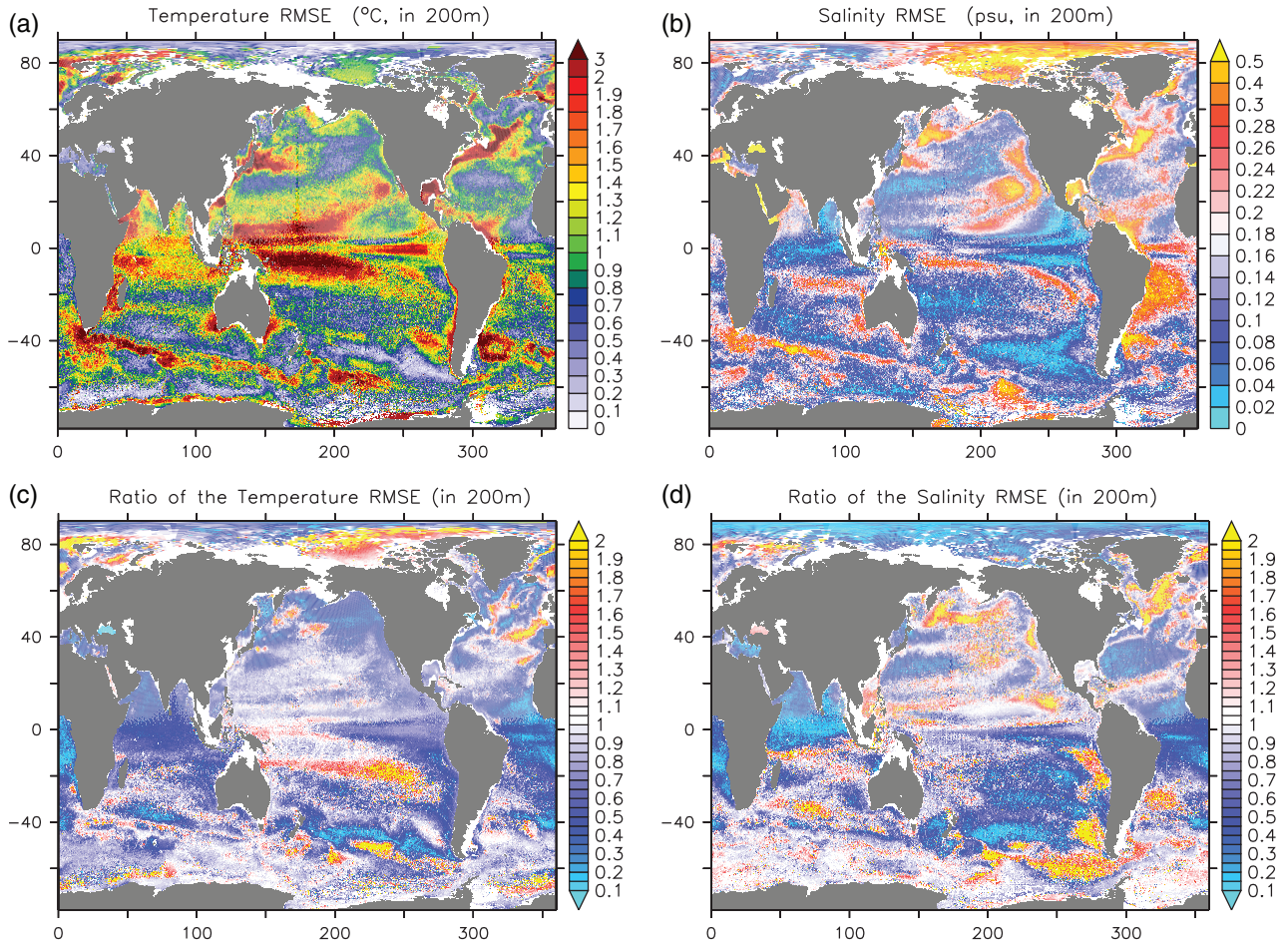

FIGURE 7 Time mean corrections to the (a) heat flux, (b) freshwater flux, and (c) zonal and (d) meridional wind stress relative to CTRL. The correction to the freshwater flux contains corrections to the river runoff as part of the changes in the precipitation, because runoff is treated identically to precipitation in the model and can therefore not be separated by the estimation procedure. Heat and freshwater fluxes include the contribution from the relaxation terms. Note the nonlinear colour scales to accommodate the high corrections in the regions of strong currents. The sign of the fluxes follow the NCEP convention with positive values into the atmosphere

and GECCO3S6m show nearly identical profiles as the almost identical cost function indicates. In comparison to GECCO2, there is an improvement for temperature in the top 200 m and at the level of the Mediterranean water visible. However, the deep ocean below 2,700 m degrades. In comparison to CTRL, most of the improvement is confined to the top 1500 m, which is also true for salinity. In comparison to GECCO2, the largest improvement of salinity takes place between 700 to 3,500 m.

6 | ESTIMATED PARAMETERS

This section is dedicated to the parameter changes that were adjusted to bring the model into consistency with the data. The mean difference of the GECCO3 fluxes relative to CTRL resulting from the changes in the atmospheric state are shown in Figure 7. Different from GECCO2, which showed large regions of positive heat flux corrections particularly in the Northern Hemisphere, adjustments are mostly characterized by regional changes in the most energetic regions. There, pattern and sign of changes agree with GECCO2. Also for the freshwater flux, the predominance of positive correction seen in GECCO2 disappears and corrections are more balanced. In the Tropics, corrections remain similar with additional freshwater input over the convergence zones, while the amplitudes are much reduced. Note that the adjustments contain the contributions from the relaxation, while the contribution from the relaxation was missing before in GECCO2's control. Mid and high latitudes are characterized by stronger evaporation. Wind stress corrections follow closely previous corrections, with largest corrections along the strong currents.

The associated standard deviation of the flux changes (not shown) also demonstrates that fluxes are predominately adjusted over regions of high oceanic variability. Large variability of freshwater flux adjustments also occurs over ice-covered regions as a consequence of changes in

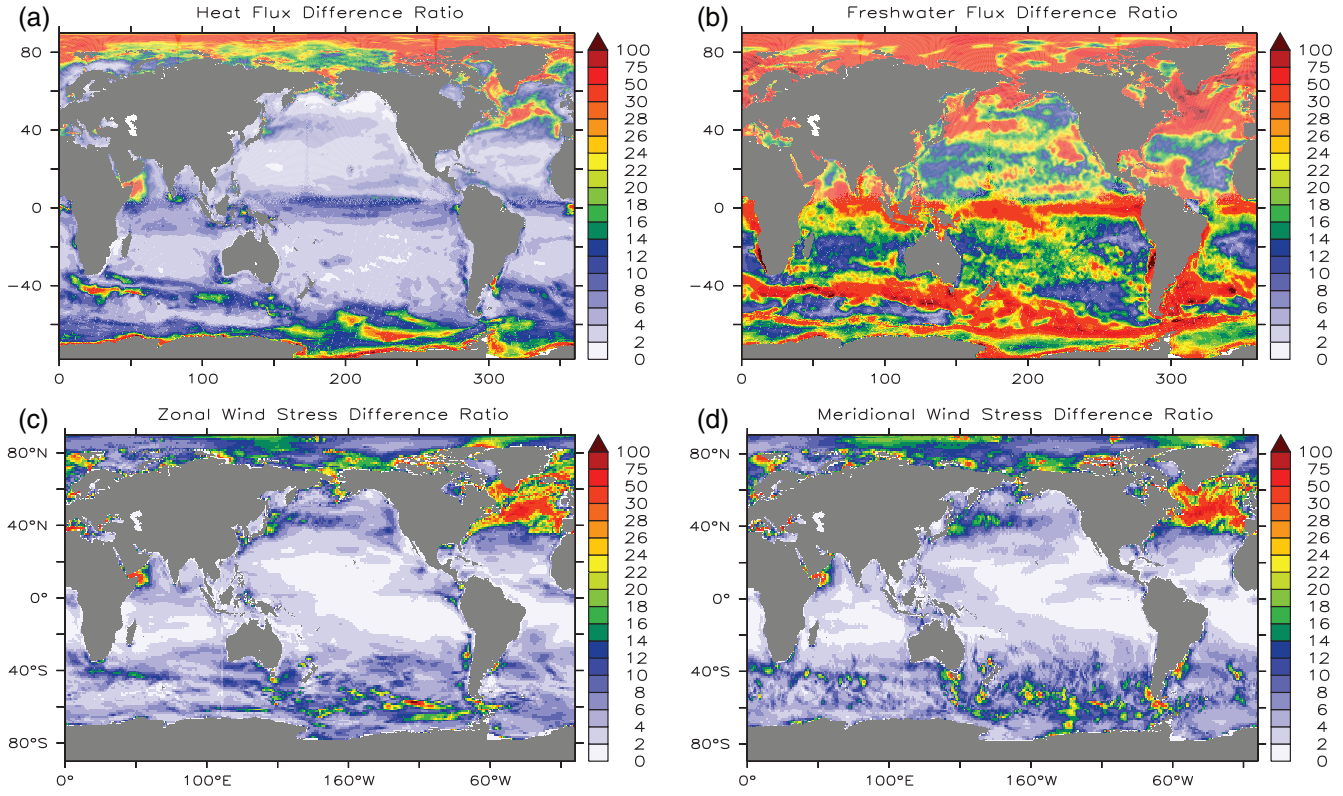

FIGURE 8 Ratio between the RMS difference in corrections of the fluxes GECCO3 minus GECCO3S6m and the RMS of the GECCO3 fluxes, for variables as in Figure 7. The fields are shown in percent to provide an estimate of the relative estimation error. Note that (b) contains the contribution from the relaxation

sea ice state. Two further regions are noteworthy. One is the region of the North Brazil Current (NBC) north of the Amazon river mouth where the freshwater plume from the Orinoco and Amazon Rivers moves with the NBC. The current retroflects near 7°N and sheds NBC rings, which reach towards the Caribbean Sea where they release freshwater (Chérubin and Richardson, 2007). Due to lack of resolution, this process is not represented by the model. A second location exists in the Bay of Bengal where runoff and transport of freshwater through the Indonesian Archipelago (Sengupta *et al.*, 2006) are important factors, which may not be sufficiently represented in CTRL – first due to the prescribed mean runoff, and second since a resolution of about 1/6° was found to be necessary to resolve the signals of the waves propagating through the passages (Lee *et al.*, 2010).

The RMS differences between the fluxes of GECCO3 and GECCO3S6m are shown in Figure 8 as percentage of the standard deviation of the respective fluxes. The patterns of differences reflect the variability of the correction with larger values over stronger currents. In these regions, differences of heat fluxes and wind stress reach 30%, while away from these regions values are typically lower than 10%. A different picture emerges for the freshwater flux; for this quantity, RMS differences are larger, reaching 50% and 20%, respectively. Since the freshwater is the only quantity that was initially perturbed by changing the relaxation time-scale, it is suggested that the differences of other fluxes were likely be larger when also perturbed.

The estimation of mixing parameters is an improvement taken over from Liu *et al.* (2012). Different from their work, the critical Richardson number was added to the set parameters but the thickness advection coefficient was removed. A further important difference is the estimation of the exponent of a multiplicative factor rather than adding the corrections, thereby avoiding negative parameters and allowing a larger range of corrections. Nevertheless, patterns of thickness diffusion correction shown in Figure 9 remain quite similar to those of Liu *et al.* (2012) and are characterized by mixing reduction along many major currents explained by mixing suppression of strong currents or potential vorticity gradients (Ferrari and Nikurashin, 2010). Other areas of reduction include the eastern, equatorward flanks of the subtropical gyres, particularly in the Northern Hemisphere, where the isopycnal diffusivity is enhanced. For the interior of the ocean, where the slopes of buoyancy and tracers can be assumed to be small, Olbers *et al.* (2012) showed that the parametrization of eddy fluxes by the GM scheme yields identical coefficients for isopycnal and thickness diffusion. The mismatch

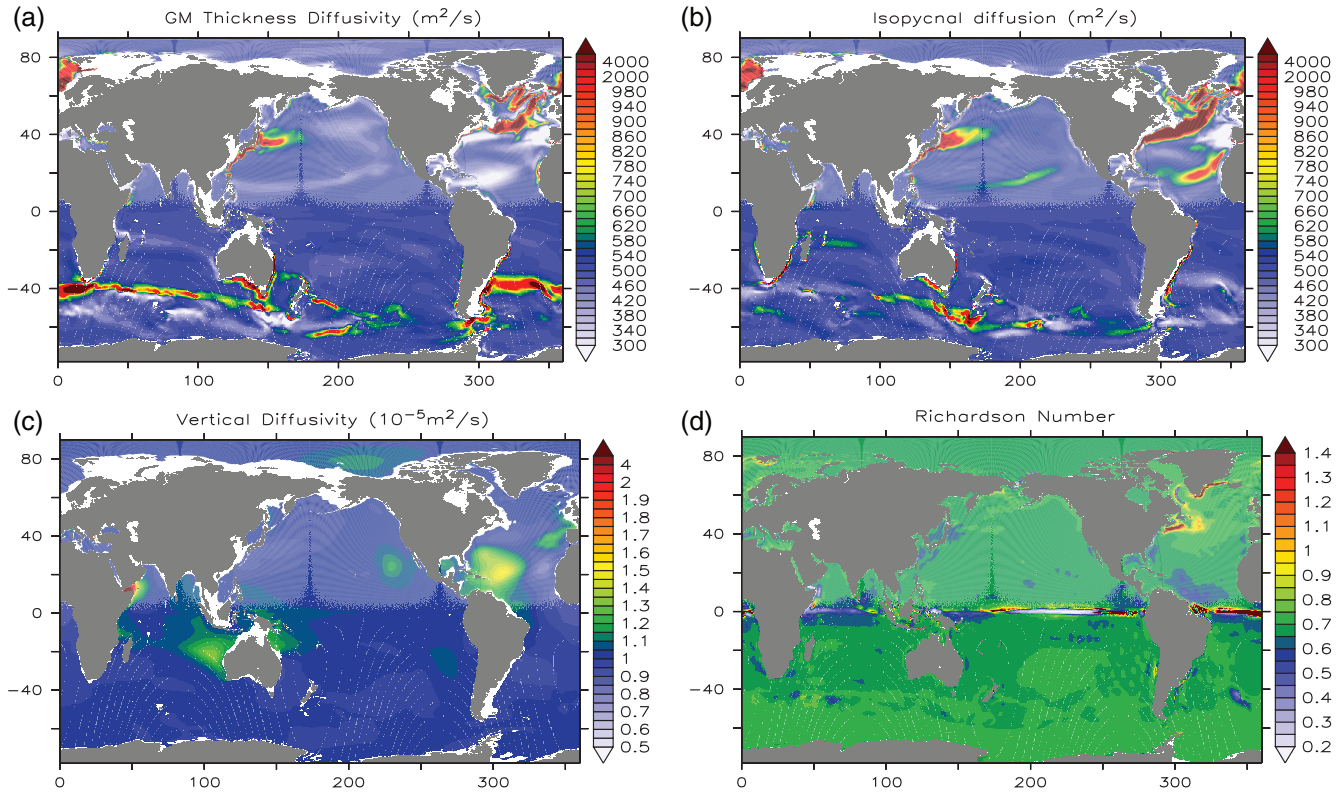

FIGURE 9 The estimated mixing parameters of (a) thickness, (b) isopycnal and (c) vertical diffusion at 400 m depth and (d) the estimated depth-independent Richardson number. The corresponding reference values for CTRL are 500, 500 $m^2 \cdot s^{-1}$, 10^{-5} $m^2 \cdot s^{-1}$ and 0.7

of the corrections for the two coefficients in the equatorward flanks of the subtropical gyres contradicts their finding. In these regions, the ratio between simulated and the observed SSH variability reaches values between 0.7 and 0.9 in comparison to ratios between 0.2 and 0.5 in frontal regions. The large eddy activity suggests that a large faction of the eddy tracer fluxes is represented by eddies rather than parametrized, which may enable both mixing coefficients to be different. Note that, according to Stammer *et al.* (2000), about 50% of the SSH variability is associated with high-frequency barotropic variability rather than eddies. Since this barotropic variability can be represented even by coarse-resolution models, the ratios of represented eddies is considerably lower than those reported here for the SSH variability, implying the absence of eddies in frontal regions and up to 50% to 80% of the eddy signal in quiet regions.

In retroflection regions in the Southern Hemisphere and along the northern flank of the ACC, enhanced thickness diffusion coincides with suppression of isopycnal mixing, which violates the findings of Olbers *et al.* (2012), despite the fact that in these areas the represented variability is low. The underlying dynamical differences are unclear, but in these areas a particularly large bias reduction was documented above.

Changes of diapycnal mixing in Figure 9c are characterized by enhanced mixing slightly poleward of 20°N/S in the eastern half of the Indian and the Pacific Ocean, which are consistent with the latitudes of tidal mixing governed by parametric subharmonic instability (MacKinnon *et al.*, 2013). In the Atlantic, a similar enhancement exists in the western half of the Northern Hemisphere while the eastern half and the Southern Hemisphere show reductions.

Adjustments to the critical *Ri* focus on the equatorial region mostly by reducing *Ri* to values as low as 0.2, thereby promoting the deepening of the mixed layer of about 5 m in the central equatorial Pacific (Figure 9). In the Atlantic, enhanced values are observed along the Equator and a reduction south of the Equator. In most other areas of the ocean, *Ri* changes are small except for a band of enhanced values that follow the East Greenland Current and Labrador Current into the Gulf Stream region. Because corrections are mostly small, the effects on the mixed-layer depth (MLD) are also expected to be small and most of the MLD changes are attributed to changes in other parameters. In comparison to the observational-based mixed-layer products by de Boyer Montegut *et al.* (2004) and Holte *et al.* (2017), the MLD of GECCO3 fits slightly better than CTRL outside polar regions but worse in regions of deep convection (not shown).

7 | THE ESTIMATED STATE

The main purpose of ocean syntheses is the analysis of the ocean circulation with respect to its climatology, variability, and change. The present section provides a few examples of such analyses and compares the results to available independent estimates to give insight into the impact of assimilating data. In particular to answer the question whether data assimilation moves the results closer to these estimates.

7.1 | Global heat content changes

During the last years the Earth's Energy Imbalance (EEI), mostly driven by anthropogenic greenhouse gas emissions, has received increasing interest. The oceans have a key role in the EEI as about 93% of the excess heat is absorbed by the oceans (Trenberth *et al.*, 2016). Measuring the heat uptake by the ocean is one of the four methods to determine EEI (Meyssignac *et al.*, 2019) and the one that is best suited on long time-scales (Von Schuckmann *et al.*, 2016). Initially, estimating the warming in the ocean (Levitus *et al.*, 2000) served to document the impact of climate change. Along with this effort, several problems with the observing system became apparent (e.g., Wijffels *et al.*, 2008; Gouretski and Reseghetti, 2010; Cheng and Zhu, 2014), which were addressed during a series of updated estimates (Domingues *et al.*, 2008; Levitus *et al.*, 2012; Cheng *et al.*, 2016; Ishii *et al.*, 2017; Zanna *et al.*, 2019). With the newer estimates, the direction of the research has changed towards understanding the EEI variability and, associated with this, the estimation of changing oceanic heating rates and detection of their uptake regions moved into focus. This new direction is partly driven by the so-called "climate change hiatus", a period between 1998 and 2013 with little change in global mean air temperatures (Allan *et al.*, 2014; Hedemann *et al.*, 2017), and the need to understand where the lack of surface warming comes from and to what extent enhanced ocean storage (e.g., Meehl *et al.*, 2011; Balmaseda *et al.*, 2013; Watanabe *et al.*, 2013) may explain it.

While previously the focus was on the upper 700 m, the lack of information from the lower layers became problematic for the attribution of changes. Newer estimates try to fill in the missing information and to provide a more detailed quantification of where heat is taken up. We follow here the separation of the full water column into different depth levels recently presented by Cheng *et al.* (2017, CEA hereafter). According to their estimate, most of the full-depth warming over the last six decades of 33.5×10^{22} J happens during the period after the mid-1980s, with the layers below 700 m accounting for about one-third of the

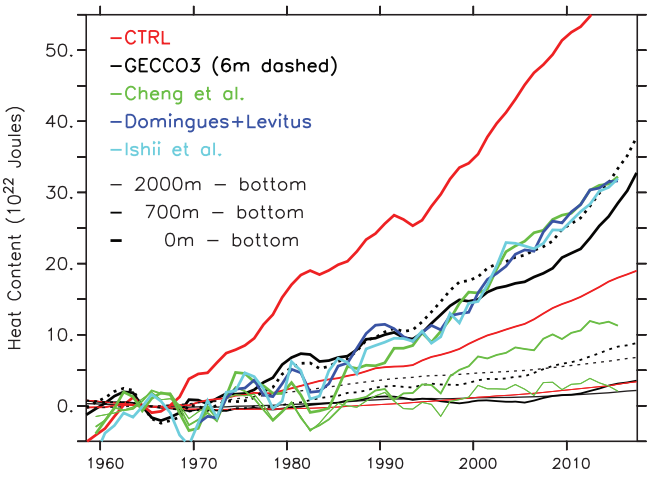

FIGURE 10 Heat content changes in the three different depth categories in comparison to CEA. The anomalies are calculated as the sum over the entire globe and with respect to the mean over the period 1960–1969. The curve Domingues+Levitus is the sum of the updated Domingues *et al.* (2008) 0–700 m plus the Levitus *et al.* (2012) 700–2,000 m estimate, which was provided together with the Ishii *et al.* (2017) estimate by Cheng *et al.* (2019a); both curves were added to the 2,000 m-to-bottom estimate by CEA to allow a comparison

warming. Nearly half of the deep-layer warming happens in layers below 2,000 m (Figure 10). While CTRL roughly matches the warming below 700 m after 1980, the comparison to GECCO3, which does not show deep-layer warming, suggests that the warming is possible only because of exaggerated warming of the layers above. The full-depth warming trend of GECCO3 roughly matches CEA until the year 2000, although it does not show the lower values of CEA during the 1980s, which are also unusually low relative to those of the combination of Domingues *et al.* (2008) plus Levitus *et al.* (2012) or Ishii *et al.* (2017). GECCO3S6m fits the independent estimates better throughout the entire period.

After 2000, GECCO3's curve flattens while in CEA warming accelerates. GECCO3's warming increases after 2010 where it now shows larger warming rates than CEA. A larger increase in those later years is in agreement with the ocean heat content deduced from the difference between altimeter and GRACE mass changes presented by Meyssignac *et al.* (2019). Deeper layers hardly pick up any heat in GECCO3 (except for the period after 2005). The comparison with GECCO3S6m shows that the estimates of the lower layers are very uncertain. The intercomparison of heat content changes from 19 different ocean reanalyses by Palmer *et al.* (2017) demonstrate a decline in agreement as the depth range moves to lower levels, with virtually no agreement below 700 m. Below 2,000 m, GECCO3S6m shows larger warming than CEA, whereas the range 700–2,000 m still does not account for

a sizeable amount of heating. The change over the total depth is larger in GECCO3S6m than GECCO3 by the deep ocean heating, which is happening mostly in the Southern Ocean, originating there particularly from the Drake Passage and the region south of the Campbell Plateau (south of New Zealand). It spreads from those places into the western parts of the Atlantic and the Pacific Oceans, respectively, similarly to those patterns shown by Purkey and Johnson (2010) for the abyssal warming below 4,000 m from the 1990s to the 2000s. The signature of the differences in deep warming is in agreement with the observation of Meehl *et al.* (2013) that greater increases of the deep ocean heat content during the hiatus periods can have a contribution from the Antarctic Bottom Water formation. Altogether these findings deem GECCO3S6m to represent ocean heat content changes more realistically than GECCO3. Although the lack of warming of GECCO3 in the layers below 2,000 m is more consistent with the small cooling trend reported by Llovel *et al.* (2014) for these layers, their estimate has an error of nearly three times the signal.

In terms of regional patterns of heat content change recently presented as anomalies for the upper 2,000 m in 2018 relative to the period 1981–2010 (Cheng *et al.*, 2019b), GECCO3 shows quite similar patterns (Figure 11). Although the shape and extent of individual patterns of positive and negative anomalies may differ between the two products, the correspondence between the patterns can be established almost everywhere. A notable difference is the strong warming of the Eurasian Basin of the Arctic Ocean that Cheng *et al.* (2019b) only indicate as a weak signal. The warming is known as the Atlantification, which consists of an increase of the heat transport into the Barents Sea caused by an increase in advection and temperature of Atlantic water (Årthun *et al.*, 2012). The associated increase in temperature gradient across the Polar Front (Barton *et al.*, 2018) is an important constraint for sea ice formation (Polyakov *et al.*, 2017). This strong warming signature is also visible in the 0–700 m heat content for 2017 shown by Johnson *et al.* (2018) relative to the 1993–2017 baseline and which shows overall similar patterns to the 0–2,000 m estimate of 2018 in Figure 11.

Regarding the climate change hiatus, the implications of the different warming rates after 2000 for GECCO3 and CEA are also quite different. While the accelerated warming of CEA supports the idea that the cooling of the atmosphere during the hiatus is caused by an enhanced heat uptake, a slowdown of the heating observed in GECCO3 is more in line with the attribution to changes in the external forcing (Kopp and Lean, 2011; Santer *et al.*, 2014). For a closer inspection of the heating rates, Figure 12 shows the intercomparison of global heat flux changes. All products show a sharp increase in heat uptake around 1998,

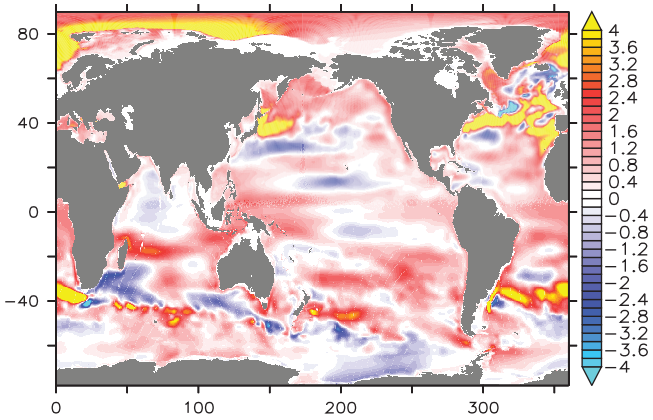

FIGURE 11 Annual mean heat content changes over 0–2,000 m for the year 2018 relative to the 1981–2010 average as shown by Cheng *et al.* (2019b). Units are $10^9 J \cdot m^{-2}$

when the warming hiatus starts. However, in the following years, the syntheses develop differently from CTRL and CEA by showing a declining uptake until 2008. For the last 20 years, CTRL shows an interdecadal variability similar to CEA while previously variability matches those of the syntheses, suggesting that, before the advent of Argo, the amount of data is not sufficient to substantially change the syntheses' heat uptake. The two syntheses differ by a multidecadal mode only: lower values of GECCOS6m before 1980 and higher values thereafter. The increase in heat uptake of the syntheses after 2014 are more in line with the increase in solar irradiance by a reduction in global mean reflected short-wave (Loeb *et al.*, 2012) than more constant values of CEA and CTRL. For completeness, we also show the global freshwater balance in Figure 12, demonstrating that the syntheses have a smaller loss of freshwater than CTRL. This loss decreases with time but shows for the syntheses a reversal of the trend at the beginning of the 2000s with the advent of the Argo data.

7.2 | Meridional heat and freshwater transports

An intercomparison of meridional heat and freshwater transports from 10 different ocean reanalyses was recently presented for the North Atlantic by Jackson *et al.* (2019) as part of a detailed analysis of the North Atlantic circulation. They found a relatively good agreement among the ocean reanalyses as well as with the observational estimates, except for a general underestimation around 26°N and except for one product which has larger values. We follow their notation and include the contribution from the GM tracer advection, mimicking the eddy heat flux, into the estimates presented for the Atlantic, Indo-Pacific and the global oceans in Figure 13. GECCO2, for which

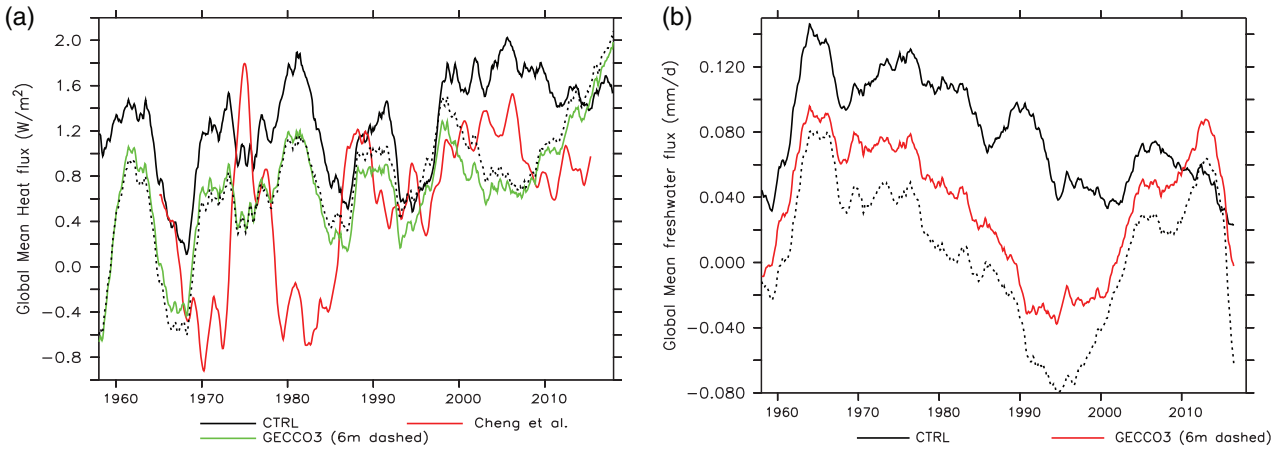

FIGURE 12 Global mean (a) net surface heat and (b) freshwater fluxes. The time series are filtered with a 60-month running mean and the freshwater flux includes the contribution from the relaxation term. Positive values mean fluxes into the ocean and the flux estimate of Cheng *et al.*, (2019a) was added

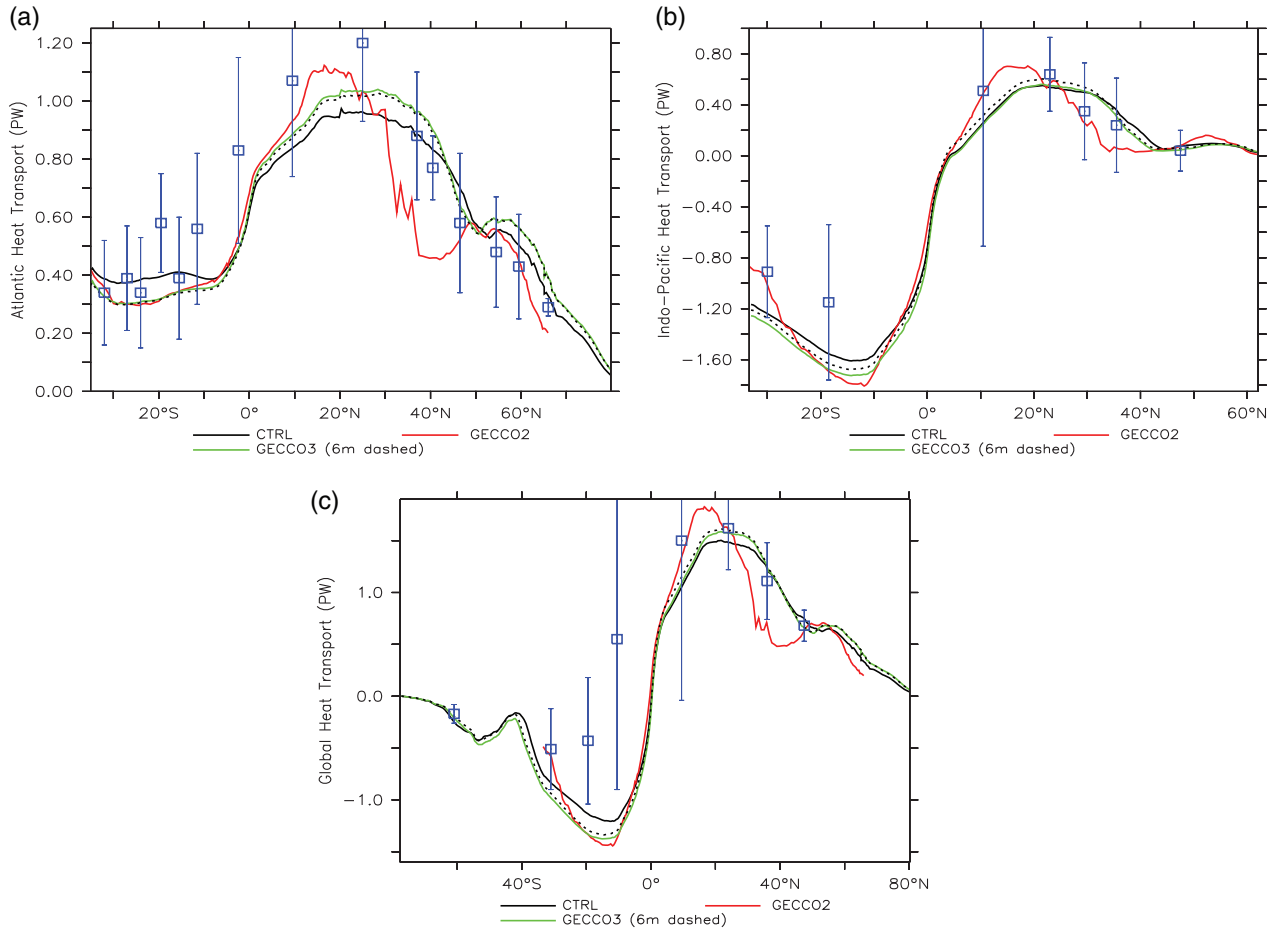

FIGURE 13 Mean meridional ocean heat transport in the (a) Atlantic, (b) Indo-Pacific and (c) global oceans from CTRL and the GECCO2 and GECCO3 syntheses. The squares are estimated from observations and data assimilation products compiled by Macdonald and Baringer (2013)

this component is not available, does not contain the fluxes but the eddy contribution typically is less than 5% of the signal. It should be noted that it is unclear to what extent the compiled independent estimates, which are included for comparison, account for the eddy heat transport component.

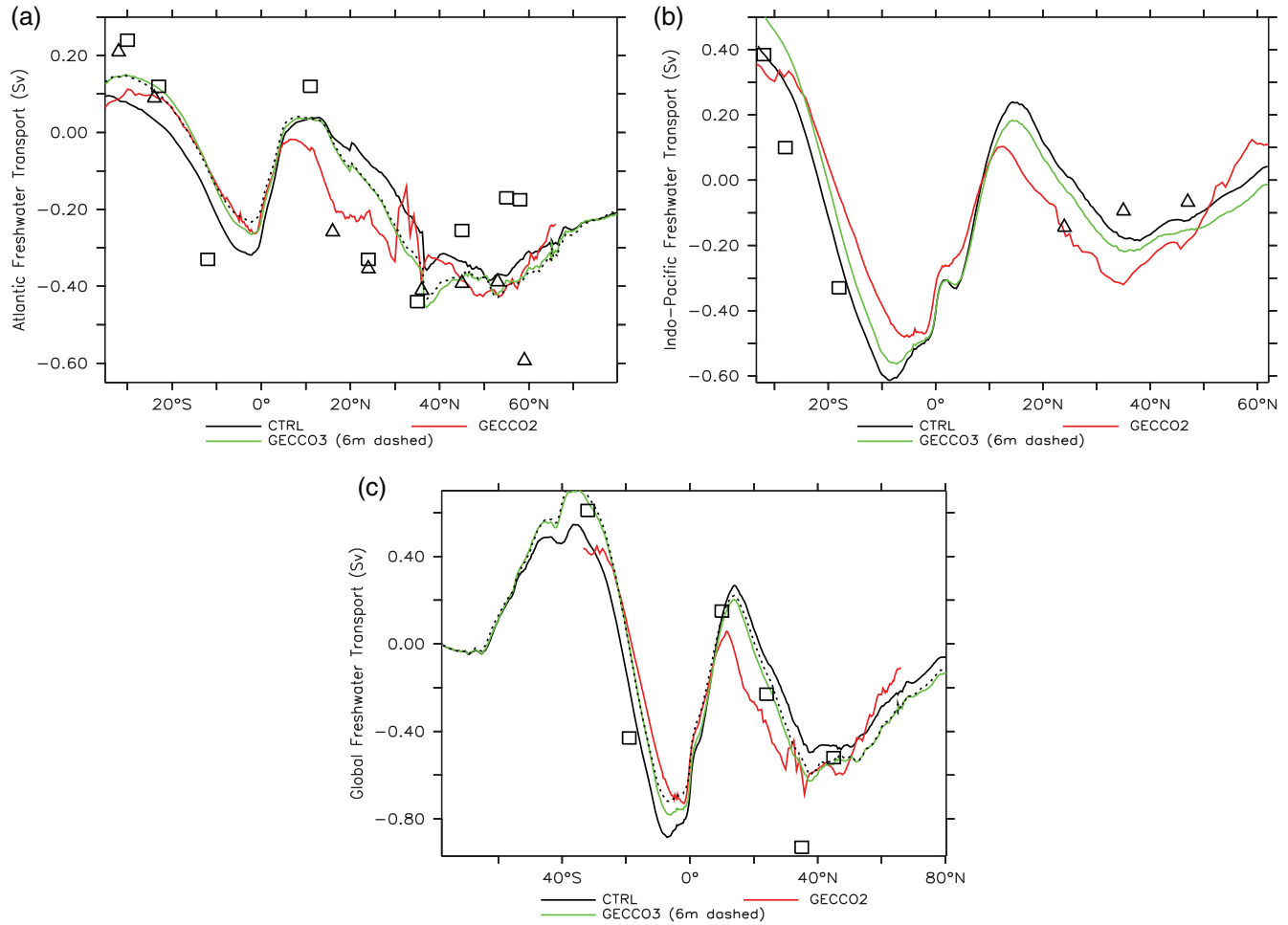

FIGURE 14 Mean meridional ocean freshwater transport in the (a) Atlantic, (b) Indo-Pacific and (c) global oceans from CTRL and the GECCO2 and GECCO3 syntheses. Estimates compiled by Talley (2008) and Wijffels *et al.*, (2001) are shown as squares and triangles, respectively

The comparison of the heat transports in the Atlantic reveals a very good agreement with the independent estimates except for an underestimation of the transports between 5°S and 26°N, where GECCO3 underestimates the independent estimates similarly to that previously reported about other products. A good agreement also holds for the Indo-Pacific, although the southward transports are overestimated in the Southern Hemisphere. Both deficiencies in the Atlantic and Pacific remain within error bars. By contrast, the global ocean transports reveal significant deficiencies in tropical regions south of the Equator despite very large error bars there.

Atlantic freshwater transports analyzed by Jackson *et al.* (2019) show the largest spread in the region of the Gulf Stream, which is mostly caused by larger southward transports of the eddy-permitting reanalyses. GECCO2 stands out as the only reanalysis that shows no northward freshwater transport in the north equatorial region. In this region, the transport is substantially altered in GECCO3 (Figure 14), which now shows a weak northward transport that still does not reach the observational estimate by Talley (2008). The southward transport further north to 30°N is also still too low. In this region, the total transport is a relatively small residual of the competing southward overturning and northward gyre components (Köhl, 2015), which makes the attribution of this deficiency difficult. In comparison to GECCO2, Indo-Pacific transports increase in amplitude in GECCO3 except for smaller values in the southward transport in the northern subtropical region. Globally the GECCO3 transports match very well the observational estimates, except for the 35°N value, which seems to be too low in the observations since the combination of the Atlantic and Indo-Pacific values of Wijffels *et al.* (2001) at 36°N and 35°N yield only −0.5 Sv. Estimates from the two GECCO3 syntheses are almost identical for heat as well as freshwater transports, suggesting that the mean state is quite robust regarding convergence problems.

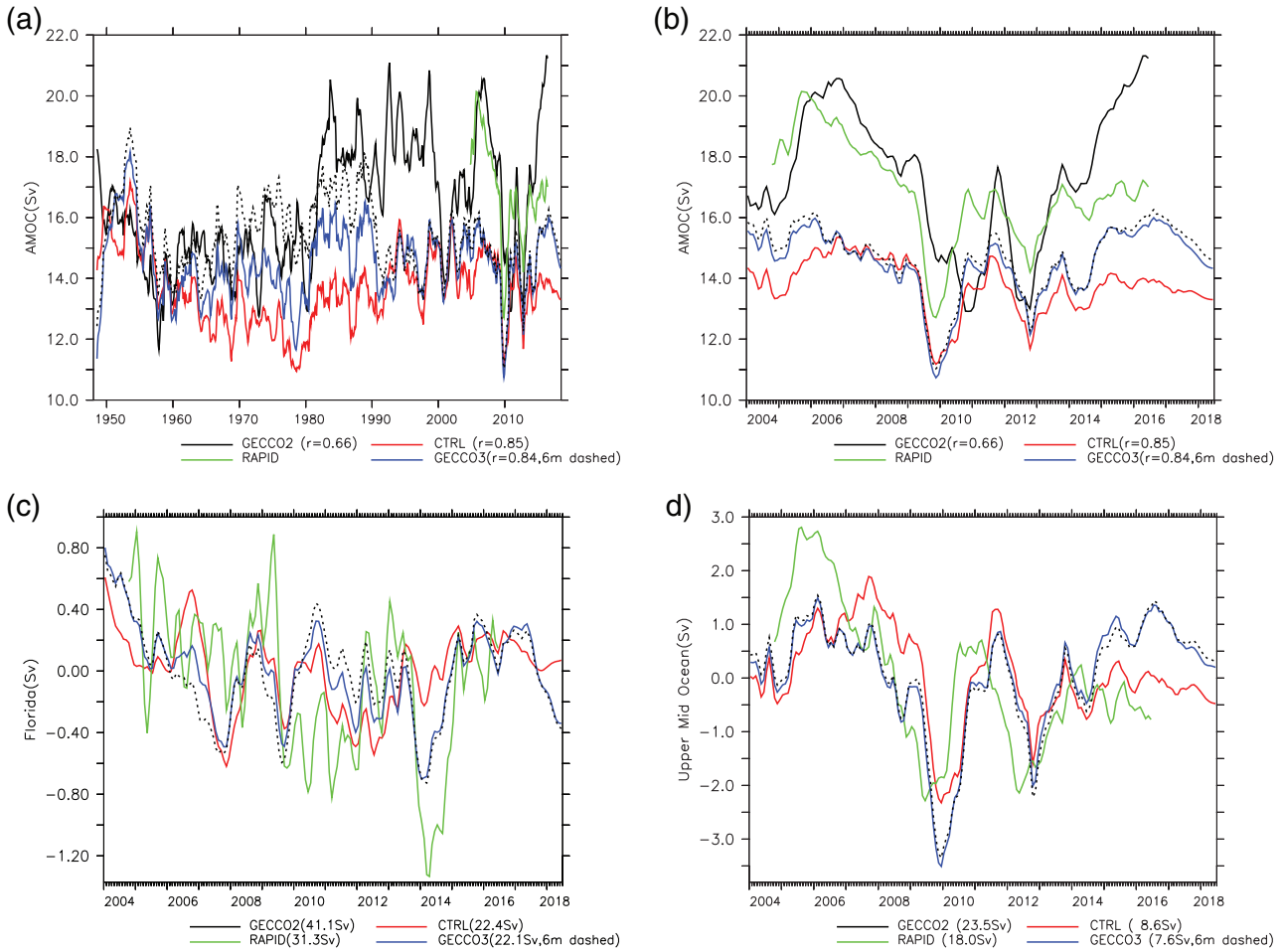

FIGURE 15 Comparison of the monthly mean transports for AMOC (in Sv) for the periods (a) 1948–2018 and (b) 2004–2018 from GECCO2 (black), CTRL (red) and the two GECCO3 syntheses (blue and dotted), with data from RAPID (green). The correlations to the AMOC from RAPID are shown in brackets. The (c) Florida Strait and (d) upper mid-ocean transports are shown as anomalies with respect to their 2005–2016 means, which are given in the brackets. GECCO2 is not shown for (c, d) because the variability is much larger than GECCO3 and RAPID

7.3 | RAPID transports

Estimates of interdecadal variability of the Atlantic Meridional Overturning (AMOC) as the key indicator for the strength of the thermohaline circulation are very uncertain and due to the lack of observations difficult to verify. Over the long time-scale of the last 60 years, only the five direct estimates by Bryden *et al.* (2005) plus the continuous time series by the RAPID-MOCHA-WBTS (RAPID-Meridional Overturning Circulation and Heat-flux Array-Western Boundary array; Smeed *et al.*, 2015; RAPID in the following) exist to validate estimates from ocean syntheses. The intercomparisons of different ocean reanalyses provided by Munoz *et al.* (2011) and Karspeck *et al.* (2017) find little consistency of the variability among the different products, in contrast to a better agreement among diversely configured simulations which were forced with a common atmospheric forcing. This suggests that the available data are insufficient to constrain the AMOC and the information entering through the assimilation creates diversity rather than providing convergence. Although agreement is a necessary condition for a small error, it is likely that the spread of a set of unconstrained, identically forced models underestimates the uncertainty. Under this assumption, one would expect increasing spread when data are added and a decreasing spread only once the solution is sufficiently constrained by data. However, the difficulty to extract information on the AMOC variability from even the RAPID *in situ* data was demonstrated by Stepanov *et al.* (2012), Köhl (2015) and Baehr (2010), although in the latter configuration forcing changes were quite inefficient, such that changes were mostly caused by the initial conditions, which mostly affected the mean. More recently, a set of reanalyses largely different from those analyzed by Karspeck *et al.* (2017) was intercompared over the period 1993–2017 by

Jackson *et al.* (2019) and revealed a good agreement for the period after 2000 and a larger divergence for the period before. This suggests a positive effect of the high data density during the Argo period, although this effect was not seen by Karspeck *et al.* (2017).

Nevertheless, as a key circulation characteristic, the AMOC at the location of the RAPID array at 26.5°N is shown in Figure 15 over the complete 71 years. At 26.5°N, the time series is close to that of the maximum AMOC. Spin-up effects are visible in all runs during the first 10 years. GECCO2 showed a clear strengthening of the AMOC particularly due to the regime shift at the beginning of the 1980s, after which the amplitude and the variability increased. In GECCO3, the shift is still visible but the strengthening from the period 1960–1980 to 1980–2018 amounts to only 1 Sv. The variability and the mean values are now lower and also lower than RAPID. The larger AMOC and Florida Strait transports in GECCO2 were a special feature of the short 5-year-long windows used by GECCO2 not seen in other syntheses such as ECCO-v4 (Wunsch and Heimbach, 2013b) or GECCO (Köhl and Stammer, 2008) which use longer windows. Differences between GECCO3 and CTRL are mostly on interdecadal time-scales. Differences between the two GECCO3 syntheses are characterized by a trend that removes the strengthening almost completely. Both GECCO3 syntheses are characterized by a maximum in AMOC during the 1980s. A closer look at the agreement with the RAPID time series demonstrates a high correlation ($r = 0.85$), which is much lower in GECCO2 because the extension years 2012–2017 did not converge well and produced a large, positive trend.

On the interannual to decadal time-scales, the variability of the GECCO3 Florida Strait Transports (FST; Figure15c) matches RAPID fairly well while on subannual to interannual time-scales there is not correspondence. The minimum in 2014 is only about half the amplitude of RAPID and the mean transport, as explained in Section 2, is reduced to about 22 Sv due to the topographic constraint. GECCO2, in comparison, has a much larger and non-matching variability (not shown because variability exceeds the plot). Similar to the AMOC, the contribution from the upper-mid-ocean transports (Figure15d) matches well except for a lag of little more than half a year which is seen for the two minima in 2009 and 2012. Due to the smaller FST, the mid-ocean transport is also reduced in GECCO3, while GECCO2 has larger values for both transports.

8 | CONCLUSIONS

The main purpose of the paper is to describe the configuration of the new version of the GECCO synthesis (GECCO3), to evaluate the success of the assimilation procedure with the assimilated data, and to demonstrate the impact on some key variables of interest by the assessment with independent estimates. Since one of the goals of the synthesis is its future use to initialize coupled climate predictions, the model was configured to be compatible with the grid and bathymetry of the high-resolution ocean component of the MPI-ESM. At a nominal resolution of 0.4°, GECCO3 is the first global eddy-permitting synthesis that employs the adjoint method to fit the model to a large variety of data over a multidecadal period, now covering 1948–2018.

GECCO3 now features the estimation of various mixing parameters, which reveal substantial changes and, differently from the MPI-ESM configuration, cause eddy fluxes parametrized by the GM parametrization to be an important part of the dynamics. The patterns of the resulting mixing coefficient remain consistent with the early estimate by Liu *et al.* (2012), which was based on a coarser model and a shorter assimilation period.

A major challenge of using the adjoint method with very long assimilation windows is the large control vector space and the associated slow convergence. In addition to this, the instability of the solution with respect to small freshwater flux perturbations was noticed to lead to premature stalling of the optimization progress and inferior solutions. The addition of relaxation boundary conditions resolves the instability problem and ensures that the initial estimate is at least as good as the control run. To test the sensitivity of the solution with respect to the relaxation time-scale, two versions of the synthesis were produced. GECCO3 uses a two-month and GECCO3S6m a six-month relaxation time-scale. Both syntheses reach almost identical levels of agreement with the data and are therefore considered as equal approximations to the optimal estimate. GECCO3S6m has a lower damping of the salinity variability but a larger RMS error relative to the climatological SSS than GECCO3. As part of an evaluation of the SSS product from the European Space Agency Sea Surface Salinity Climate Change Initiative (Boutin *et al.*, 2019), the SSS product was assimilated as part of shorter syntheses over the period 2011–2018 which were started from GECCO3 and GECCO3S6m, respectively. The initial SSS cost functions revealed a 10% lower weighted RMS error for GECCO3S6m, suggesting its better representation of the SSS variability during at least the data-rich Argo period.

Overall, the fit to the data is better than for the previous GECCO2 synthesis, partly related to the larger amount of Argo data. Despite the additional adjustment of the mixing parameters, patterns of biases remain similar to those of GECCO2 but a reduction is observed in regions of large mixing adjustments.

Estimating the Earth's energy imbalance is a challenging problem. This difficulty is reflected by the uncertainty of the estimate below 2,000 m related to perturbing the state of the optimization at iteration 10. Although the total changes of GECCO3S6m fit into the range of other estimates, unlike other products, little heat is taken up by the layers between 700 and 2,000 m. After around year 2000, GECCO3 shows lower total changes than GECCO3S6m and almost no heating below 2,000 m, which is only supported by the very uncertain estimates of Llovel *et al.* (2014). In contrast GECCO3S6m's patterns of heating below 2,000 m for the last years agree with recent observations (Purkey and Johnson, 2010) and a warming hiatus (Meehl *et al.*, 2013). The differences between GECCO3 and GECCO3S6m suggest that the available heat content information from the data does not sufficiently constrain the changes. However, perturbing the freshwater flux has very little impact on the mean meridional heat and freshwater transport estimates or variability on interannual or shorter time-scales.

The small advantages of GECCO3S6m over GECCO3, shown for SSS and ocean heat content, lead to the weak recommendation to use GECCO3S6m, particularly because the lower damping of GECCO3S6m is closer to real ocean physics.

The obvious way to the future is to aim for eddy-resolving syntheses. While for sequential assimilation methods operational global products at 1/12° resolution exist (Cummings, 2005; Lellouche *et al.*, 2018), they so far cover only little more than a decade. Although the feasibility of employing the adjoint method for realistic eddy-permitting syntheses over time-scales beyond the predictability limit was demonstrated early by Köhl and Willebrand (2002), global, eddy-resolving syntheses over multidecadal time-scales are still far out of reach. Products closest to that goal are for instance the two-year synthesis for the Southern Ocean at 1/6° presented by Mazloff *et al.* (2010) and regional eddy-resolving versions at 1/10° to 1/16° (Gopalakrishnan *et al.*, 2013; Zaba *et al.*, 2018), which however cover only the relatively small domains of the Gulf of Mexico/California Current and have assimilation windows of only a few months. The problem of convergence over long time-windows and the large elapsed time to perform the synthesis prevents fast progress.

ACKNOWLEDGEMENTS

AK acknowledges support from the RACE-Synthese project funded by the German Ministry for Education and Research (BMBF). The HadISST and the EN.4.2.1 data were obtained from http://www.metoffice.gov.uk. The mapped and along-track altimeter data were downloaded from http://marine.copernicus.eu through their ftp site. Frank Siegismund provided the combination of the GOCO05s geoid with the DTU10 mean sea surface height. Data from the World Ocean Atlases are provided by http://www.nodc.noaa.gov and the NCEP data by http://www.esrl.noaa.gov. Sea ice concentration was obtained from http://osisaf.met.no and provided by EUMETSAT Ocean and Sea Ice Satellite Application Facility at the Norwegian and Danish Meteorological Institutes. The sea surface salinity was obtained from the Natural Environment Research Council's Data Repository for Atmospheric Science and Earth Observation at http://catalogue.ceda.ac.uk (all accessed 27 March 2020).

ORCID

Armin Köhl https://orcid.org/0000-0002-9777-674X

REFERENCES

Adcroft, A., Campin, J.-M., Heimbach, P., Hill, C. and Marshall, J. (2002). MITgcm Release. http://mitgcm.org/sealion/; accessed27March2020

Allan, R.P., Liu, C., Loeb, N.G., Palmer, M.D., Roberts, M., Smith, D. and Vidale, P.-L. (2014) Changes in global net radiative imbalance 1985–2012. *Geophysical Research Letters*, 41, 5588–5597

Andersen, O.B. (2010). The DTU10 Gravity field and Mean sea surface in Second international symposium of the gravity field of the Earth (IGFS2), 20–22 September 2010, Fairbanks, Alaska. https://www.space.dtu.dk/english/Research/Scientific_data_and_models/Global_Marine_Gravity_Field; accessed 27 March 2020).

Årthun, M., Eldevik, T., Smedsrud, L., Skagseth, Ø. and Ingvaldsen, R. (2012) Quantifying the influence of Atlantic heat on Barents Sea ice variability and retreat. *Journal of Climate*, 25, 4736–4743

Baehr, J. (2010) Influence of the 26°N RAPID-MOCHA array and Florida current cable observations on the ECCO-GODAE state estimate. *Journal of Physical Oceanography*, 40, 865–879

Balmaseda, M.A., Hernandez, F., Storto, A., Palmer, M., Alves, O., Shi, L., Smith, G., Toyoda, T., Valdivieso, M., Barnier, B., Behringer, D., Boyer, T., Chang, S.Y., Chepurin, A.G., Ferry, N., Forget, G., Fujii, Y., Good, S., Guinehut, S., Haines, K., Ishikawa, Y., Keeley, S., Köhl, A., Lee, T., Martin, J.M., Masina, S., Masuda, S., Meyssignac, B., Mogensen, K., Parent, L., Peterson, A.K., Tang, M.Y., Yin, Y., Vernieres, G., Wang, X., Waters, J., Wedd, R., Wang, O., Xue, Y., Chevallier, M., Lemieux, F.J., Dupont, F., Kuragano, T., Kamachi, M., Awaji, T., Caltabiano, A., Wilmer-Becker, K. and Gaillard, F. (2015) The ocean reanalyses intercomparison project (ORA-IP). *Journal of Operational Oceanography*, 8, s80–s97

Balmaseda, M.A., Trenberth, K.E. and Källén, E. (2013) Distinctive climate signals in reanalysis of global ocean heat content. *Geophysical Research Letters*, 40, 1754–1759

Barton, B.I., Lenn, Y.-D. and Lique, C. (2018) Observed Atlantification of the Barents Sea causes the Polar Front to limit the expansion of winter sea ice. *Journal of Physical Oceanography*, 48, 1849–1866

Boutin, J., Vergely, J.-L., Koehler, J., Rouffi, F. and Reul, N. (2019). ESA Sea surface salinity climate change initiative (Sea_Surface_Salinity_cci): monthly sea surface salinity product v1.8. Centre for Environmental Data Analysis, Chilton, UK.

de Boyer Montegut, C., Madec, G., Fischer, A.S., Lazar, A. and Iudicone, D. (2004) Mixed layer depth over the global ocean: an examination of profile data and a profile-based climatology. *Journal of Geophysical Research: Oceans*, 1978–2012, 109

Bryan, F. (1986a) High-latitude salinity effects and interhemispheric thermohaline circulations. *Nature*, 323, 301–304

Bryan, F. (1986b). Maintenance and variability of the thermohaline circulation. PhD thesis, Princton University, Princeton, NJ.

Bryden, H.L., Longworth, H.R. and Cunningham, S.A. (2005) Slowing of the Atlantic meridional overturning circulation at 25°N. *Nature*, 436, 655–657

Cheng, L., Abraham, J., Hausfather, Z. and Trenberth, K.E. (2019a) How fast are the oceans warming?. *Science*, 363, 128–129

Cheng, L., Trenberth, K.E., Fasullo, J., Boyer, T., Abraham, J. and Zhu, J. (2017) Improved estimates of ocean heat content from 1960 to 2015. *Science Advances*, 3. https://doi.org/10.1126/sciadv.1601545

Cheng, L., Trenberth, K.E., Palmer, M.D., Zhu, J. and Abraham, J.P. (2016) Observed and simulated full-depth ocean heat content changes for 1970–2005. *Ocean Science*, 12, 925–935

Cheng, L. and Zhu, J. (2014) Artifacts in variations of ocean heat content induced by the observation system changes. *Geophysical Research Letters*, 41, 7276–7283

Cheng, L., Zhu, J., Abraham, J., Trenberth, K.E., Fasullo, J.T., Zhang, B., Yu, F., Wan, L., Chen, X. and Song, X. (2019b) 2018 Continues record global ocean warming. *Advances in Atmospheric Sciences*, 36, 249–252

Chérubin, L. and Richardson, P.L. (2007) Caribbean current variability and the influence of the Amazon and Orinoco freshwater plumes. *Deep Sea Research Part I: Oceanographic Research Papers*, 54, 1451–1473

Chevallier, M., Smith, G.C., Dupont, F., Lemieux, J.-F., Forget, G., Fujii, Y., Hernandez, F., Msadek, R., Peterson, K.A., Storto, A., Toyoda, T., Valdivieso, M., Vernieres, G., Zuo, H., Balmaseda, M., Chang, Y.-S., Ferry, N., Garric, G., Haines, K., Keeley, S., Kovach, R.M., Kuragano, T., Masina, S., Tang, Y., Tsujino, H. and Wang, X. (2017) Intercomparison of the Arctic sea ice cover in global ocean–sea ice reanalyses from the ORA-IP project. *Climate Dynamics*, 49, 1107–1136

Cummings, J.A. (2005) Operational multivariate ocean data assimilation. *Quarterly Journal of the Royal Meteorological Society*, 131, 3583–3604

Domingues, C., Church, J., White, N., Gleckler, P., Wijffels, S., Barker, P. and Dunn, J. (2008) Improved estimates of upper-ocean warming and multi-decadal sea-level rise. *Nature*, 453, 1090–1093

Eden, C., Greatbatch, R.J. and Willebrand, J. (2007) A diagnosis of thickness fluxes in an eddy-resolving model. *Journal of Physical Oceanography*, 37, 727–742

Fekete, B.M., Vörösmarty, C.J. and Grabs, W. (2002) High-resolution fields of global runoff combining observed river discharge and simulated water balances. *Global Biogeochemical Cycles*, 16(3). https://doi.org/10.1029/1999GB001254.

Ferrari, R. and Nikurashin, M. (2010) Suppression of eddy diffusivity across jets in the Southern Ocean. *Journal of Physical Oceanography*, 40, 1501–1519

Ferreira, D., Marshall, J. and Heimbach, P. (2005) Estimating eddy stresses by fitting dynamics to observations using a residual-mean ocean circulation model and its adjoint. *Journal of Physical Oceanography*, 35, 1891–1910

Forget, G., Campin, J.-M., Heimbach, P., Hill, C.N., Ponte, R.M. and Wunsch, C. (2015) ECCO version 4: an integrated framework for non-linear inverse modeling and global ocean state estimation. *Geoscientific Model Development*, 8, 3071–3104

Galanti, E. and Tziperman, E. (2003) A midlatitude–ENSO teleconnection mechanism via baroclinically unstable long Rossby waves. *Journal of Physical Oceanography*, 33, 1877–1888

Gent, P.R. and McWilliams, J. (1990) Isopycnal mixing in ocean circulation models. *Journal of Physical Oceanography*, 20, 150–155

Gilbert, J.C. and Lemaréchal, C. (1989) Some numerical experiments with variable-storage quasi-Newton algorithms. *Mathematical Programming*, 45, 407–435

Giorgetta, M.A., Jungclaus, J., Reick, C.H., Legutke, S., Bader, J., Böttinger, M., Brovkin, V., Crueger, T., Esch, M., Fieg, K. and et al. (2013) Climate and carbon cycle changes from 1850 to 2100 in MPI-ESM simulations for the Coupled Model Intercomparison Project phase 5. *Journal of Advances in Modeling Earth Systems*, 5, 572–597

Good, S.A., Martin, M.J. and Rayner, N.A. (2013) EN4: Quality controlled ocean temperature and salinity profiles and monthly objective analyses with uncertainty estimates. *Journal of Geophysical Research: Oceans*, 118, 6704–6716

Gopalakrishnan, G., Cornuelle, B.D., Hoteit, I., Rudnick, D.L. and Owens, W.B. (2013) State estimates and forecasts of the loop current in the Gulf of Mexico using the MITgcm and its adjoint. *Journal of Geophysical Research: Oceans*, 118, 3292–3314

Gouretski, V. and Reseghetti, F. (2010) On depth and temperature biases in bathythermograph data: Development of a new correction scheme based on analysis of a global ocean database. *Deep Sea Part I*, 57, 812–833

Gregg, M. (1987) Diapycnal mixing in the thermocline: a review. *Journal of Geophysical Research: Oceans*, 92, 5249–5286

Hallberg, R. (2013) Using a resolution function to regulate parameterizations of oceanic mesoscale eddy effects. *Ocean Modelling*, 72, 92–103

Hedemann, C., Mauritsen, T., Jungclaus, J. and Marotzke, J. (2017) The subtle origins of surface-warming hiatuses. *Nature Climate Change*, 7, 336

Holte, J., Talley, L.D., Gilson, J. and Roemmich, D. (2017) An Argo mixed layer climatology and database. *Geophysical Research Letters*, 44, 5618–5626

Ishii, M., Fukuda, Y., Hirahara, S., Yasui, S., Suzuki, T. and Sato, K. (2017) Accuracy of global upper ocean heat content estimation expected from present observational data sets. *SOLA*, 13, 163–167

Jackson, L.C., Dubois, C., Forget, G., Haines, K., Harrison, M., Iovino, D., Kohl, A., Mignac, D., Masina, S., Peterson, K.A., Piecuch, C., Roberts, C., Robson, J., Storto, A., Toyoda, T., Valdivieso, M., Wilson, C., Wang, Y. and Zuo, H. (2019) The mean state and variability of the North Atlantic circulation: a perspective from ocean reanalyses. *Journal of Geophysical Research: Oceans*, 124, 9142–9170. https://doi.org/10.1029/2019JC015210

Jiang, Z., Hui, W. and Kamachi, M. (2002) The improvement made by a modified TLM in 4DVAR with a geophysical boundary-layer model. *Advances in Atmospheric Sciences*, 19, 563–582

Johnson, G.C., Lyman, J.M., Boyer, T., Cheng, L., Domingues, C.M., Gilson, J., Ishii, M., Killick, R., Monselesan, D., Purkey, S.G. and Wijffels, S.E. (2018) Ocean heat content in State of the Climate in 2017. *Bulletin of the American Meteorological Society*, 99, S72–S77

Jungclaus, J., Fischer, N., Haak, H., Lohmann, K., Marotzke, J., Matei, D., Mikolajewicz, U., Notz, D. and Von Storch, J. (2013)

Characteristics of the ocean simulations in the Max Planck Institute Ocean Model (MPIOM), the ocean component of the MPI-Earth system model. *Journal of Advances in Modeling Earth Systems*, 5, 422–446

Kalmikov, A.G. and Heimbach, P. (2014) A Hessian-based method for uncertainty quantification in global ocean state estimation. *SIAM Journal on Scientific Computing*, 36, S267–S295

Kalnay, E., Kanamitsu, M., Kistler, R., Collins, W., Gandin, D.D.L., Iredell, M., Saha, S., White, G., Woollen, J., Zhu, Y., Chelliah, M., Ebisuzaki, W., Higgins, W., Janowiak, J., Mo, K.C., Ropelewski, C., Leetmaa, A., Reynolds, R. and Jenne, R. (1996) The NCEP/NCAR 40-year re-analysis project. *Bulletin of the American Meteorological Society*, 77, 437–471

Karspeck, A.R., Stammer, D., Köhl, A., Danabasoglu, G., Balmaseda, M.A., Smith, D.M., Fujii, Y., Zhang, S., Giese, B., Tsujino, H. and Rosati, A. (2017) Comparison of the Atlantic meridional overturning circulation between 1960 and 2007 in six ocean reanalysis products. *Climate Dynamics*, 49, 957–982

Köhl, A. (2005) Anomalies of meridional overturning: mechanisms in the North Atlantic. *Journal of Physical Oceanography*, 35, 1455–1472

Köhl, A. (2015) The GECCO2 ocean synthesis: transports of volume, heat and freshwater in the North Atlantic. *Quarterly Journal of the Royal Meteorological Society*, 141, 166–181. https://doi.org/10.1002/qj.2347

Köhl, A., Siegismund, F. and Stammer, D. (2012) Impact of assimilating bottom pressure anomalies from GRACE on ocean circulation estimates. *Journal of Geophysical Research*, 117(C4). https://doi.org/10.1029/2011JC007623

Köhl, A. and Stammer, D. (2008) Variability of the meridional overturning in the North Atlantic from the 50 years GECCO state estimation. *Journal of Physical Oceanography*, 38, 1913–1930

Köhl, A. and Willebrand, J. (2002) An adjoint method for the assimilation of statistical characteristics into eddy-resolving ocean models. *Tellus A*, 54, 406–425

Kopp, G. and Lean, J.L. (2011) A new, lower value of total solar irradiance: evidence and climate significance. *Geophysical Research Letters*, 38(1). https://doi.org/10.1029/2010GL045777

Kröger, J., Pohlmann, H., Sienz, F., Marotzke, J., Baehr, J., Köhl, A., Modali, K., Polkova, I., Stammer, D., Vamborg, F.S. and Müller, W.A. (2018) Full-field initialized decadal predictions with the MPI earth system model: an initial shock in the North Atlantic. *Climate Dynamics*, 51, 2593–2608

Kunze, E., Firing, E., Hummon, J.M., Chereskin, T.K. and Turnherr, A.M. (2006) Global abyssal mixing inferred from lowered ADCP shear and CTD strain profiles. *Journal of Physical Oceanography*, 36, 1553–1576

Large, W.G. and Yaeger, S.G. (2004). Diurnal to decadal global forcing for ocean and sea-ice models: the data sets and flux climatologies. Technical Note TN-460+STR, NCAR, Boulder, CO.

Large, W.G., Williams, J.C. and Doney, S.C. (1994) Ocean vertical mixing: a review and a model with a nonlocal boundary-layer parametrization. *Reviews of Geophysics*, 32, 363–403

Lee, T., Awaji, T., Balmaseda, M., Ferry, N., Fujii, Y., Fukumori, I., Giese, B., Heimbach, P., Köhl, A., Masina, S., Remy, E., Rosati, A., Schodlok, M.P., Stammer, D. and Weaver, A.T. (2010) Consistency and fidelity of Indonesian-throughflow total volume transport estimated by 14 ocean data assimilation products. *Dynamics of Atmospheres and Oceans*, 50, 201–223. https://doi.org/10.1016/j.dynatmoce.2009.12.004

Lellouche, J.-M., Greiner, E., Galloudec, O.L., Garric, G., Regnier, C., Drevillon, M., Benkiran, M., Testut, C.-E., Bourdalle-Badie, R., Gasparin, F., Hernandez, O., Levier, B., Drillet, Y., Remy, E. and Le Traon, P.-Y. (2018) Recent updates to the Copernicus Marine Service global ocean monitoring and forecasting real-time 1/12° high-resolution system. *Ocean Science*, 14, 1093–1126. https://doi.org/10.5194/os-14-1093-2018

Levitus, S., Antonov, J.I., Boyer, T.P. and Stephens, C. (2000) Warming of the world ocean. *Science*, 287, 2225–2229

Levitus, S., Antonov, J.I., Boyer, T.P., Baranova, O.K., Garcia, H.E., Locarnini, R.A., Mishonov, A.V., Reagan, J.R., Seidov, D., Yarosh, E.S. and Zweng, M.M. (2012) World ocean heat content and thermosteric sea level change (0–2000 m), 1955–2010. *Geophysical Research Letters*, 39(10). https://doi.org/10.1029/2012GL051106

Liu, C., Köhl, A. and Stammer, D. (2012) Adjoint-based estimation of eddy-induced tracer mixing parameters in the global ocean. *Journal of Physical Oceanography*, 42, 1186–1206

Llovel, W., Willis, J.K., Landerer, F.W. and Fukumori, I. (2014) Deep-ocean contribution to sea level and energy budget not detectable over the past decade. *Nature Climate Change*, 4, 1031–1035

Locarnini, R., Mishonov, A., Antonov, J., Boyer, T., Garcia, H., Baranova, O., Zweng, M., Paver, C., Reagan, J., Johnson, D., Hamilton, M. and Seidov, D. (2013) *World Ocean Atlas 2013, Volume 1: Temperature*. Levitus, S., Mishonov, A. (eds), NOAA Atlas, NESDIS, Silver Spring, MA.

Locarnini, R., Mishonov, A., Baranova, O., Boyer, T., Zweng, M., Garcia, H., Reagan, J., JR Seidov D., Weathers, C., Paver, C. and Smolyar, I. (2018) *World Ocean Atlas 2018, Volume 1: Temperature*. Mishonov, A. (ed.), NOAA Atlas, NESDIS, Silver Spring, MA.

Loeb, N.G., Lyman, J.M., Johnson, G.C., Allan, R.P., Doelling, D.R., Wong, T., Soden, B.J. and Stephens, G.L. (2012) Observed changes in top-of-the-atmosphere radiation and upper-ocean heating consistent within uncertainty. *Nature Geoscience*, 5, 110–113

Losch, M., Menemenlis, D., Campin, J.-M., Heimbach, P. and Hill, C. (2010) On the formulation of sea-ice models. Part 1: effects of different solver implementations and parameterizations. *Ocean Modelling*, 33, 129–144

Macdonald, A.M. and Baringer, M.O. (2013). Ocean heat transport, pp. 759–785 in Ocean circulation & Climate: a 21st century perspective. International Geophysics Series, Vol. 103, Academic Press, Cambridge, MA.

MacKinnon, J.A., Alford, M.H., Sun, O., Pinkel, R., Zhao, Z. and Klymak, J. (2013) Parametric subharmonic instability of the internal tide at 29°N. *Journal of Physical Oceanography*, 43, 17–28

Masuda, S., Awaji, T., Sugiura, N., Matthews, J.P., Toyoda, T., Kawai, Y., Doi, T., Kouketsu, S., Igarashi, H., Katsumata, K., Uchida, H., Kawano, T. and Fukasawa, M. (2010) Simulated rapid warming of abyssal North Pacific waters. *Science*, 329, 319–322. https://doi.org/10.1126/science.1188703

Mazloff, M.R., Heimbach, P. and Wunsch, C. (2010) An eddy-permitting Southern Ocean state estimate. *Journal of Physical Oceanography*, 40, 880–899

Meehl, G.A., Arblaster, J.M., Fasullo, J.T., Hu, A. and Trenberth, K.E. (2011) Model-based evidence of deep-ocean heat uptake during surface-temperature hiatus periods. *Nature Climate Change*, 1, 360

Meehl, G.A., Hu, A., Arblaster, J.M., Fasullo, J. and Trenberth, K.E. (2013) Externally forced and internally generated decadal climate variability associated with the Interdecadal Pacific Oscillation. *Journal of Climate*, 26, 7298–7310

Meyssignac, B., Boyer, T., Zhao, Z., Hakuba, M.Z., Landerer, F.W., Stammer, D., Köhl, A., Kato, S., L'Ecuyer, T., Ablain, M., Abraham, J.P., Blazquez, A., Cazenave, A., Church, J.A., Cowley, R., Cheng, L., Domingues, C.M., Giglio, D., Gouretski, V., Ishii, M., Johnson, G.C., Killick, R.E., Legler, D., Llovel, W., Lyman, J., Palmer, M.D., Piotrowicz, S., Purkey, S.G., Roemmich, D., Roca, R., Savita, A., von Schuckmann, K., Speich, S., Stephens, G., Wang, G., Wijffels, S.E. and Zilberman, N. (2019) Measuring global ocean heat content to estimate the earth energy imbalance. *Frontiers in Marine Science*, 6. https://doi.org/10.3389/fmars.2019.00432

Moum, J.N., Lien, R.-C., Perlin, A., Nash, J.D., Gregg, M.C. and Wiles, P.J. (2009) Sea surface cooling at the Equator by subsurface mixing in tropical instability waves. *Nature Geoscience*, 2, 761–765

Munoz, E., Kirtman, B. and Weijer, W. (2011) Varied representation of the Atlantic meridional overturning across multidecadal ocean reanalyses. *Deep Sea Research Part II. Topical Studies in Oceanography*, 58, 1848–1857

Olbers, D., Willebrand, J. and Eden, C. (2012) *Ocean dynamics*. Springer, Berlin.

Pail, R., Goiginger, H., Schuh, W.-D., Höck, E., Brockmann, J., Fecher, T., Gruber, T., Mayer-Gürr, T., Kusche, J., Jäggi, A. and Rieser, D. (2010) Combined satellite gravity field model GOCO01S derived from GOCE and GRACE. *Geophysical Research Letters*, 37(20). https://doi.org/10.1029/2010GL044906

Palmer, M., Roberts, C., Balmaseda, M., Chang, Y.-S., Chepurin, G., Ferry, N., Fujii, Y., Good, S., Guinehut, S., Haines, K. and et al. (2017) Ocean heat content variability and change in an ensemble of ocean reanalyses. *Climate Dynamics*, 49, 909–930

Polyakov, I.V., Pnyushkov, A.V., Alkire, M.B., Ashik, I.M., Baumann, T.M., Carmack, E.C., Goszczko, I., Guthrie, J., Ivanov, V.V., Kanzow, T., Krishfield, R., Kwok, R., Sundfjord, A., Morison, J., Rember, R. and Yulin, A. (2017) Greater role for Atlantic inflows on sea-ice loss in the Eurasian Basin of the Arctic Ocean. *Science*, 356, 285–291. https://doi.org/10.1126/science.aai8204

Purkey, S.G. and Johnson, G.C. (2010) Warming of global abyssal and deep Southern Ocean waters between the 1990s and 2000s: contributions to global heat and sea level rise budgets. *Journal of Climate*, 23, 6336–6351

Rayner, N.A., Parker, D.E., Horton, E.B., Folland, C.K., Alexander, L.V., Rowell, D.P., Kent, E.C. and Kaplan, A. (2003) Global analyses of sea surface temperature, sea ice, and night marine air temperature since the late nineteenth century. *Journal of Geophysical Research: Atmospheres*, 108(D14). https://doi.org/10.1029/2002JD002670

Redi, M.H. (1982) Oceanic isopycnal mixing by coordinate rotation. *Journal of Physical Oceanography*, 12, 1154–1158

Santer, B.D., Bonfils, C., Painter, J.F., Zelinka, M.D., Mears, C., Solomon, S., Schmidt, G.A., Fyfe, J.C., Cole, J.N., Nazarenko, L., Taylor, K.E. and Wentz, F.J. (2014) Volcanic contribution to decadal changes in tropospheric temperature. *Nature Geoscience*, 7, 185–189. https://doi.org/10.1038/ngeo2098

Sengupta, D., Bharath Raj, G.N. and Shenoi, S.S.C. (2006) Surface freshwater from Bay of Bengal runoff and Indonesian throughflow in the tropical Indian Ocean. *Geophysical Research Letters*, 33(22). https://doi.org/10.1029/2006GL027573

Shi, L., Alves, O., Wedd, R., Balmaseda, M., Chang, Y., Chepurin, G., Ferry, N., Fujii, Y., Gaillard, F., Good, S., Guinehut, S., Haines, K., Hernandez, F., Lee, T., Palmer, M., Peterson, K.A., Masuda, S., Storto, A., Toyoda, T., Valdivieso, M., Vernieres, G., Wang, X. and Yin, Y. (2017) An assessment of upper ocean salinity content from the Ocean Reanalyses Intercomparison Project (ORA-IP). *Climate Dynamics*, 49, 1009–1029

Smeed, D., McCarthy, G., Rayner, D., Moat, B.I., Johns, W.E., Baringer, M.O. and Meinen, C.S. (2015). Atlantic meridional overturning circulation observed by the RAPID-MOCHA-WBTS (RAPID–Meridional Overturning Circulation and Heatflux Array–Western Boundary Time Series) array at 26N from 2004 to 2015. British Oceanographic Data Centre, NERC, Liverpool, UK. doi:10/6qb.

Smyth, W., Moum, J., Li, L. and Thorpe, S. (2013) Diurnal shear instability, the descent of the surface shear layer, and the deep cycle of equatorial turbulence. *Journal of Physical Oceanography*, 43, 2432–2455

Speer, K. and Forget, G. (2013) Global distribution and formation of mode waters. *International Geophysics*, 103, 211–226

Stammer, D. (1998) Toward an estimate of the global circulation from WOCE data and a general circulation model. *International WOCE Newsletter*, 31, 7–9

Stammer, D., Wunsch, C. and Ponte, R.M. (2000) De-aliasing of global high-frequency barotropic motions in altimeter observations. *Geophysical Research Letters*, 27, 1175–1178

Stepanov, V.N., Haines, K. and Smith, G.C. (2012) Assimilation of RAPID array observations into an ocean model. *Quarterly Journal of the Royal Meteorological Society*, 138, 2105–2117

Storto, A., Masina, S., Balmaseda, M., Guinehut, S., Xue, Y., Szekely, T., Fukumori, I., Forget, G., Chang, Y.-S., Good, S.A., Köhl, A., Vernieres, G., Ferry, N., Andrew Peterson, K., Behringer, D., Ishii, M., Masuda, S., Fujii, Y., Toyoda, T., Yin, Y., Valdivieso, M., Barnier, B., Boyer, T., Lee, T., Gourrion, J., Wang, O., Heimback, P., Rosati, A., Kovach, R., Hernandez, F., Martin, M.J., Kamachi, M., Kuragano, T., Mogensen, K., Alves, O., Haines, K. and Wang, X. (2017) Steric sea level variability (1993–2010) in an ensemble of ocean reanalyses and objective analyses. *Climate Dynamics*, 49, 709–729

Sugiura, N., Awaji, T., Masuda, S., Mochizuki, T., Toyoda, T., Miyama, T., Igarashi, H. and Ishikawa, Y. (2008) Development of a four-dimensional variational coupled data assimilation system for enhanced analysis and prediction of seasonal to interannual climate variations. *Journal of Geophysical Research; Oceans*, 113(C10). https://doi.org/10.1029/2008JC004741

Talley, L.D. (2008) Freshwater transport estimates and the global overturning circulation: shallow, deep and throughflow components. *Progress in Oceanography*, 78, 257–303

Thacker, W.C. (1989) The role of the Hessian matrix in fitting models to measurements. *Journal of Geophysical Research: Oceans*, 94, 6177–6196

Toyoda, T., Fujii, Y., Kuragano, T., Kamachi, M., Ishikawa, Y., Masuda, S., Sato, K., Awaji, T., Hernandez, F., Ferry, N., Guinehut, S., Martin, M.J., Andrew Peterson, K., Good, S.A., Valdivieso, M., Haines, K., Storto, A., Masina, S., Köhl, A., Zuo, H., Balmaseda, M., Yin, Y., Shi, L., Alves, O., Smith, G., Chang, Y.-S., Vernieres, G., Wang, X., Forget, G., Heimbach, P., Wang, O., Fukumori, I. and Lee, T. (2017) Intercomparison and validation

of the mixed-layer depth fields of global ocean syntheses. *Climate Dynamics*, 49, 753–773

Trenberth, K.E., Fasullo, J.T., Von Schuckmann, K. and Cheng, L. (2016) Insights into Earth's energy imbalance from multiple sources. *Journal of Climate*, 29, 7495–7505

Valdivieso, M., Haines, K., Balmaseda, M.A., Chang, Y.-S., Drevillon, M., Ferry, N., Fujii, Y., Köhl, A., Storto, A., Toyoda, T., Wang, X., Waters, J., Xue, Y., Yin, Y., Barnier, B., Hernandez, F., Kumar, A., Lee, T., Masina, S. and Andrew Peterson, K. (2017) An assessment of air–sea heat fluxes from ocean and coupled reanalyses. *Climate Dynamics*, 49, 983–1008

Von Schuckmann, K., Palmer, M., Trenberth, K.E., Cazenave, A., Chambers, D., Champollion, N., Hansen, J., Josey, S., Loeb, N., Mathieu, P.-P., Meyssignac, B. and Wild, M. (2016) An imperative to monitor earth's energy imbalance. *Nature Climate Change*, 6, 138

Watanabe, M., Kamae, Y., Yoshimori, M., Oka, A., Sato, M., Ishii, M., Mochizuki, T. and Kimoto, M. (2013) Strengthening of ocean heat uptake efficiency associated with the recent climate hiatus. *Geophysical Research Letters*, 40, 3175–3179

Wijffels, S.E., Toole, J.M. and Davis, R. (2001) Revisiting the South Pacific Subtropical circulation: a synthesis of World Ocean Circulation Experiment observations along 32°S. *Journal of Geophysical Research; Atmospheres*, 106, 19481–19513. https://doi.org/10.1029/1999JC000118

Wijffels, S.E., Willis, J., Domingues, C.M., Barker, P., White, N.J., Gronell, A., Ridgway, K. and Church, J.A. (2008) Changing expendable bathythermograph fall rates and their impact on estimates of thermosteric sea level rise. *Journal of Climate*, 21, 5657–5672. https://doi.org/10.1175/2008JCLI2290.1

Wunsch, C. and Heimbach, P. (2013a) Dynamically and kinematically consistent global ocean circulation and ice state estimates. *International Geophysics*, 103, 553–579

Wunsch, C. and Heimbach, P. (2013b) Two decades of the Atlantic meridional overturning circulation: anatomy, variations, extremes, prediction, and overcoming its limitations. *Journal of Climate*, 26, 7167–7186

Zaba, K.D., Rudnick, D.L., Cornuelle, B.D., Gopalakrishnan, G. and Mazloff, M.R. (2018) Annual and interannual variability in the California current system: comparison of an ocean state estimate with a network of underwater gliders. *Journal of Physical Oceanography*, 48, 2965–2988

Zanna, L., Khatiwala, S., Gregory, J.M., Ison, J. and Heimbach, P. (2019) Global reconstruction of historical ocean heat storage and transport. *Proceedings of the National Academy of Sciences*, 116, 1126–1131

Zedler, S., Jackson, C., Yao, F., Heimbach, P., Köhl, A., Scott, R.B. and Hoteit, I. (2016). Calibration of the K-profile parameterization of ocean boundary layer mixing. Part I: development. arXiv: 1604.05802.

Zweng, M.M., Reagan, J.R., Antonov, J.I., Locarnini, R.A., Mishonov, A.V., Boyer, T.P., Garcia, H.E., Baranova, O.K., Johnson, D.R., Seidov, D. and Biddle, M.M. (2013) *World Ocean Atlas 2013. Volume 2, Salinity*. Levitus, S., Mishonov, A. (eds), NOAA Atlas, NESDIS, Silver Spring, MA.

Zweng, M.M., Reagan, J.R., Seidov D., Boyer, T.P., Locarnini, R.A., Garcia, H.E., Mishonov, A.V., Baranova, O.K., Weathers, K., Paver, C.R. and Smolyar, I. (2018) *World Ocean Atlas 2018. Volume 2, Salinity*. Mishonov, A. (ed.), NOAA Atlas, NESDIS, Silver Spring, MA.

How to cite this article: Köhl A. Evaluating the GECCO3 1948–2018 ocean synthesis – a configuration for initializing the MPI-ESM climate model. *Q J R Meteorol Soc*. 2020;146:2250–2273. https://doi.org/10.1002/qj.3790